ORNL/TM-2022/2381
NFE-19-07887

Computational Fluid Dynamics Simulations to Predict Oxidation in Heat Recovery Steam Generator Tubes

Nithin S. Panicker
Marc-Olivier G. Delchini
Thomas Sambor
Adrian S. Sabau

March 2022

ORNL IS MANAGED BY UT-BATTELLE LLC FOR THE US DEPARTMENT OF ENERGY

DOCUMENT AVAILABILITY

Reports produced after January 1, 1996, are generally available free via OSTI.GOV.

Website www.osti.gov

Reports produced before January 1, 1996, may be purchased by members of the public from the following source:

National Technical Information Service
5285 Port Royal Road
Springfield, VA 22161
Telephone 703-605-6000 (1-800-553-6847)
TDD 703-487-4639
Fax 703-605-6900
E-mail info@ntis.gov
Website http://classic.ntis.gov/

Reports are available to DOE employees, DOE contractors, Energy Technology Data Exchange representatives, and International Nuclear Information System representatives from the following source:

Office of Scientific and Technical Information
PO Box 62
Oak Ridge, TN 37831
Telephone 865-576-8401
Fax 865-576-5728
E-mail reports@osti.gov
Website https://www.osti.gov/

This report was prepared as an account of work sponsored by an agency of the United States Government. Neither the United States Government nor any agency thereof, nor any of their employees, makes any warranty, express or implied, or assumes any legal liability or responsibility for the accuracy, completeness, or usefulness of any information, apparatus, product, or process disclosed, or represents that its use would not infringe privately owned rights. Reference herein to any specific commercial product, process, or service by trade name, trademark, manufacturer, or otherwise, does not necessarily constitute or imply its endorsement, recommendation, or favoring by the United States Government or any agency thereof. The views and opinions of authors expressed herein do not necessarily state or reflect those of the United States Government or any agency thereof.

ORNL/TM-2021/2381
NFE-19-07887

Nuclear Energy and Fuel Cycle Division

COMPUTATIONAL FLUID DYNAMICS SIMULATIONS TO PREDICT OXIDATION IN HEAT RECOVERY STEAM GENERATOR TUBES

Nithin S. Panicker*
Marc-Olivier G. Delchini*
Thomas Sambor†
Adrian S. Sabau*

---

* Oak Ridge National Laboratory
†Electric Power Research Institute

March 2022

Prepared by
OAK RIDGE NATIONAL LABORATORY
Oak Ridge, TN 37831
managed by
UT-BATTELLE LLC
for the
US DEPARTMENT OF ENERGY
under contract DE-AC05-00OR22725

CONTENTS

LIST OF FIGURES iv
LIST OF TABLES v
ABBREVIATIONS vi
NOMENCLATURE vi
ABSTRACT 1
1. STATEMENT OF OBJECTIVES 2
  1.1 INTRODUCTION 2
  1.2 COMPUTATIONAL FLUID DYNAMICS SIMULATION OF HRSG: A REVIEW 2
  1.3 PROPOSED APPROACH 3
2. BENEFITS OF FUNDING DOE OFFICE’S MISSION 4
3. TECHNICAL DISCUSSION OF WORK PERFORMED BY ALL PARTIES 5
  3.1 PRELIMINARY CFD MODEL DEVELOPMENT, VERIFICATION, AND PREDICTIONS 5
    3.1.1 Oxidation Model 5
    3.1.2 Computational Fluid Dynamics Model of an HRSG 6
    3.1.3 Prediction of the oxide thickness for with-fin and without-fin cases using realistic thermal conditions for the HRSG 10
  3.2 MODELING THE IMPACT OF THE FINS ON THE HEAT TRANSFER AND PRESSURE DROP USING A POROUS MEDIA MODEL 12
    3.2.1 The Porous Media Model 13
    3.2.2 Modeling of Pressure Drop and Heat Transfer Using the Porous Media Model 13
    3.2.3 Procedure to Optimize the Forchheimer and the Heat Transfer Parameters 13
    3.2.4 Numerical Results from the Porous Media Model 14
    3.2.5 Comments on the PMM Approach 19
  3.3 REYNOLDS-AVERAGED NAVIER-STOKES SIMULATION OF THE REAL-SCALE HRSG AND OXIDE THICKNESS PREDICTION 20
    3.3.1 Computational Fluid Dynamics Model 20
    3.3.2 Geometry and Computational Mesh 22
    3.3.3 Tuning of Porous Media Parameters to Match Field Test Data 24
    3.3.4 Results and Discussion 25
4. COMMERCIALIZATION POSSIBILITIES 36
5. PLANS FOR FUTURE COLLABORATION 36
6. CONCLUSIONS 37
  6.1 PHASE 1: VERIFICATION AND VALIDATION OF THE CFD MODEL ON REDUCED-SCALE GEOMETRIES 37
  6.2 PHASE 2: MODEL DEVELOPMENT TO CAPTURE THE FIN EFFECT ON THE OXIDE THICKNESS 37
  6.3 PHASE 3: INVESTIGATION OF FLOW, HEAT TRANSFER, AND OXIDATION IN A REAL-SCALE HRSG 38
7. REFERENCES 39

LIST OF FIGURES

Figure 1. Comparison of oxide evolution: STAR-CCM+ vs. analytical solution..6
Figure 2. CAD model with fins (left) and without fins (right). 7
Figure 3. Mesh on a cut plane. 8
Figure 4. Mesh on a vertical plane perpendicular to the gas flow cutting the tubes. 9
Figure 5. Temperature on a cut section plane parallel to the flow with fins (left) and without fins (right). 10
Figure 6. Velocity on a cut section plane parallel to the flow with fins (left) and without fins (right). 10
Figure 7. Oxide thickness Ugas = 4 m/s with fins (left) and without fins (right). 11
Figure 8. Oxide thickness Ugas = 16 m/s with fins (left) and without fins (right). 11
Figure 9. Average oxide thickness on all the tubes with and without fins for different inlet gas velocities over multiple years. 12
Figure 10. CAD model showing how the fin regions are approximated by a porous region. 12
Figure 11. Gas velocity profile obtained using with-fin model. 15
Figure 12. Gas velocity profile obtained using PMM. 16
Figure 13. Gas temperature profile obtained using the with-fin model. 16
Figure 14. Gas temperature profile obtained using PMM. 17
Figure 15. Temperature profile of the inner surface pipes obtained using with-fin model. 17
Figure 16. Temperature profile of the inner surface pipes obtained using PMM. 18
Figure 17. CAD model of real-scale half-HRSG. 21
Figure 18. Top view of the HX tubes considered for oxidation study. 22
Figure 19. Mesh on a vertical plane perpendicular to the gas flow cutting the tubes. 23
Figure 20. Mesh on a horizontal plane parallel to the gas flow cutting the tubes. 23
Figure 21. Flow pattern in the inlet duct of the HRSG: perspective view (a) and side view (b). 25
Figure 22. Flow UI on different planes in the flow direction. 26
Figure 23. 3D gas flow vector on a plane cutting the tubes at the center of the HRSG. 27
Figure 24. 3D gas flow vector across the tubes on a plane cutting the tubes at the top of the HRSG. 27
Figure 25. Velocity contour across the tubes. 28
Figure 26. Streamlines. 28
Figure 27. Temperature drops across tubes while exhaust heat is being harvested. 29
Figure 28. Temperature distribution on a plane in front of the HPSH1 tubes. 29
Figure 29. Gas velocity on the lower side of the HRSG. 30
Figure 30. Gas temperature on the lower side of the HRSG. 30
Figure 31. Oxide thickness profile along a tube in the HPSH1 section (top) and oxide thickness contour on each tube of HPSH1 section (bottom). 31
Figure 32. Oxide thickness profile along a tube in the RHTR1 section (left) and oxide thickness contour on each tube of RHTR1 section (right). 32
Figure 33. Oxide thickness profile along a tube in the RHTR2 section (left) and oxide thickness contour on each tube of RHTR2 section (right). 32
Figure 34. Oxide thickness profile along a tube in the HPSH2 section (left) and oxide thickness contour on each tube of HPSH2 section (right). 33

LIST OF TABLES

Table 1. Convergence grid indices for the oxide thickness 6
Table 2. Comparison of quantities obtained from the CFD simulation of fins vs. the experiment 9
Table 3. Comparison of pressure drops and heat transfer between the with-fin CFD model and the PMM for the HPSH1 14
Table 4. Comparison of pressure drops and heat transfer between the with-fin CFD model and the PMM for the HPSH2 14
Table 5. Comparison of pressure drop and heat transfer between the with-fin CFD model and the PMM for the RHSH1 14
Table 6. Comparison of pressure drops and heat transfer between the with-fin CFD model and the PMM for the RHSH2 14
Table 7. Thermophysical properties....20
Table 8. Inlet flow conditions of HRSG operated by Vogt power 20
Table 9. Comparison of CFD vs. test data for outlet tube temperature 24
Table 10. Porous coefficients used to match the test data 24
Table 11. Forchheimer parameters....24

ABBREVIATIONS

AMO	Advanced Manufacturing Office
CAD	computer-aided design
CFD	computational fluid dynamics
GCI	grid convergence indices
GUI	graphical user interface
DOE	US Department of Energy
EERE	Office of Energy Efficiency and Renewable Energy
EPRI	Electric Power Research Institute
GT	gas turbine
HPC	high-performance computing
HPC4mtls	High-Performance Computing for Materials
HPSH	high-pressure superheater [tube]
HRSG	heat recover steam generator
HX	heat exchanger, defined as a collection of tubes inside the HRSG
NEAMS	Nuclear Energy Advanced Modeling and Simulation
ORNL	Oak Ridge National Laboratory
PM	porous media
PMM	porous media model
RANS	Reynolds-averaged Navier Stokes
RHTR	reheater
SST	sheer stress transport
UI	uniformity index

NOMENCLATURE

p	pressure ($\mathrm{N/m^2}$)
u	velocity ($\mathrm{m/s}$)
T	temperature (K)
k	turbulent kinetic energy ($\mathrm{m^2/s^2}$)
ρ	density ($\mathrm{kg/m^3}$)
μ	dynamic viscosity (Pa - s)
Cp	heat capacity ($\mathrm{J/Kg\ K}$)
k	thermal conductivity ($\mathrm{W/m\ K}$)
g	gravity ($\mathrm{m/s^2}$)

ABSTRACT

Heat recovery steam generators (HRSGs) are widely used across the United States in combined cycle power plants to recover waste heat from the gas turbine. HRSGs are used to generate electricity or to produce process steam for industrial applications. The primary components of an HRSG are a duct and a heat exchanger (HX). It is known across the power industry that high-temperature oxidation, ensuing exfoliation, and subsequent solid particle erosion (SPE) can result in significant damage to components downstream (in the direction of steam flow) of the HRSG. Alloys and/or coatings to prevent or mitigate oxidation are very expensive, so they must be used or applied on targeted regions of the HX tubes where oxide formation is likely to occur. The main goal of this project is to identify these regions through computational fluid dynamics (CFD) simulations. A CFD framework was developed using the commercial code STAR-CCM+ to predict the fluid flow and heat transfer in an HRSG and associated oxidation inside the HX tubes. The developed CFD framework was verified and validated with experimental data before deployment. Furthermore, an innovative method was developed to model the effect of the HX tube fins on the heat transfer and the pressure drop using a porous media model (PMM) approach to keep the mesh size within reasonable limits. After validation, high-fidelity CFD simulations of a real-scale HRSG were performed using the PMM and the high performance computing resources at Oak Ridge National Laboratory. The simulation results were used to acquire oxide thickness maps for all the tubes of the select HX sections of HRSG prone to oxidation. These oxide maps can inform regions of the HX tubes that require oxide-resistant coatings or alloys, thereby guiding engineers for cost-efficient manufacturing of the HX to combat oxidation and subsequent exfoliation in HRSGs.

1. STATEMENT OF OBJECTIVES

1.1 INTRODUCTION

Solid particle erosion caused by steam-side oxide exfoliation is a widespread industry issue that occurs in numerous components situated downstream (in the direction of steam flow) from heat recovery steam generators (HRSGs). Affected components include but are not limited to drain lines, valve components, and steam turbine components. During design, limits are imposed on the maximum temperature of HRSGs for strength considerations—not for preventing the exfoliation of steam-side oxides. The practice of using 9Cr steels (e.g., Grade 91 alloy) at these temperatures is questionable because of its steam-side oxidation and exfoliation behavior.

HRSG exchangers (HXs) are typically created from bundles of tubes called *harps* or *coils*, the design of which typically relies on a combination of fundamental heat transfer theory and decades-old empirical correlations based on their geometry. So far, existing design methodologies have proven conducive when determining the steam temperature leaving a particular HX; indeed, the steam temperature leaving the HRSG may not require any conditioning to meet the intended target temperature, thus demonstrating the validity of this design methodology. Although the average steam temperature leaving each HX may be as intended, steam temperatures within individual tubes in the HX may be higher or lower than the average steam temperature. The variation in steam temperature and metal wall temperature within an HRSG can be affected by factors such as tube shape, HRSG thermal design, gas turbine (GT) design, condition of the HRSG and GT, and HRSG-GT operating practices. The effect of each factor on temperatures remains largely unquantified, so there is a need to determine the locations where temperatures may be elevated.

This study was conducted to gain an understanding of steam-side oxidation in HX tubes in which generated steam is superheated and reheated. This project focused on the effect of steady-state flow (full or partial load) and heat transfer on the oxide thickness growth and the ensuing exfoliation. The objective is to quantify the extent of oxide growth and its most prevalent locations, because exfoliation is expected to occur once critical oxide thicknesses are reached (EPRI, 2017). To accomplish these objectives, an advanced computational fluid dynamics (CFD)–thermal model was required to accurately model thermal-hydraulic and oxidation phenomena within the HRSG. With access to high-performance computing (HPC) resources, CFD simulations can be used to investigate each of these effects at the level of detail required. CFD can be used to analyze the spatial resolution required to quantify the phenomena described above with the accuracy needed. Detailed modeling of the thermal-hydraulics is valuable for determining the HRSG areas where (1) nominal 9Cr steels can be used without concern of oxidation/exfoliation within a reasonable operational lifetime, and (2) more oxide-resistant, potentially new or repurposed alloys would be more suitable.

1.2 COMPUTATIONAL FLUID DYNAMICS SIMULATION OF HRSG: A REVIEW

The computational cost needed to resolve the conjugate heat transfer problem over the HRSG's entire HX assembly (e.g., tubes and tube spacings) is very high. Hence, CFD simulations are often implemented in a porous media (PM) approach in which the HX assemblies are modeled as a porous media with empirical porous coefficients: porosity, porous resistance coefficients, and thermal sink terms. Moreover, most of the CFD studies that adopt this approach revolve around improving exhaust gas uniformity on the HXs to achieve maximum heat absorption. Yuwono and Widodo (Yuwono & Widodo, 2021) performed CFD studies using the PM approach to improve the exhaust gas flow uniformity in an HRSG. They concluded that the introduction of a turning vane in the inlet duct of the HRSG can improve flow uniformity, thereby increasing heat absorption. Moreover, the PM approach enabled them to conduct a CFD study at a low computational cost. Hegde et. al. (Hegde, Han, Lee, & Roy, 2007) conducted a study to improve the gas uniformity on the HXs using a PM CFD approach. They validated their simulation results with the experimental flow data acquired from a 1/15-scale model of the HRSG. The design changes suggested that placing perforated plates in front of the high-pressure superheater resulted in improved gas uniformity. Shin et al. (Shin, Kim, Ahn, Choi, & Myoung, 2012) used PM CFD to evaluate various design ideas that could improve exhaust gas flow uniformity. They performed qualitative validation of their CFD model prediction, with the experimental study conducted on a reduced-scale HRSG model. They found out that the placement of perforated plates at the inlet duct of the real-scale HRSG improved flow uniformity significantly, which is also consistent with the findings of Hedge et al. (Hegde, Han, Lee, & Roy, 2007). So et al. (So, Jo, Lee, Koo, & Lee, 2018) used a PM CFD model coupled with meta-heuristic design algorithm to search the optimum duct geometry design to maximize the exhaust gas uniformity. The optimized duct geometry determined from their study showed a recirculation zone at the top wall which improved the velocity uniformity.

The porous coefficients required for the PM approach can also be calculated through reduced scale HRSG CFD simulations. Torresi et al. (Torresi, Saponaro, Camporeale, & Fortunato, 2008) performed a CFD investigation to determine the porous resistance coefficients on a reduced scale geometry of the HRSG's HX tubes. The tube spacings and inlet conditions were varied, and the inertial and viscous porous resistance coefficients were calculated for each configuration. Based on the data acquired through CFD simulations, a correlation was developed for the porous resistance coefficients, and they applied it to simulate a real-scale HRSG with HXs stacked in the flow direction. A preliminary assessment of the flow prediction from the real-scale HRSG simulation helped to define reasonable behavior of the developed correlation for porous coefficients.

Because of the high computational cost, the literature does not include results from CFD studies that resolve issues with the tubes. Khoshhal et al. (Khosshal, Rahimi, Gharamani, & Alsairafi, 2011) performed a CFD study to assess the capability of a novel combustion technique (reduced emission) for preheating the exhaust gas for improved heat extraction by the superheater steam tubes. The CFD model in their study accounts for the exhaust gas flow in a real HRSG, but the study is limited to steam flow through a single tube of the superheater HX module. They concluded that the selection of nozzle position and the amount of the fuel injected had a significant effect on heat extraction.

1.3 PROPOSED APPROACH

It is evident from the literature review that the approach followed to model the HRSG using CFD was primarily based on PM. In the PM approach, regions with exhaust gas flowing around finned tubes are modeled as a porous medium: that is, the finned tubes are not resolved, and source/sink terms are used to simulate the effect of fins on the pressure and heat transfer model. The primary goal of this work is to predict oxide growth inside the tubes as discussed above. The growth of the oxide inside a steam tube is controlled by the convective heating of the individual tubes by the exhaust gas flow, and the convective cooling of the individual tubes by the steam flowing inside the tubes; therefore, the prediction of oxide growth requires adequate flow resolution inside and around the steam tubes, which is not feasible using a PM approach. The simulation using the PM approach also effects the prediction of flow uniformity over the HX assemblies, which is a key parameter in optimizing heat recovery from the exhaust gas. This study proposes an alternative approach to (1) resolve the exhaust gas flow in the HX tube gaps, (2) resolve the steam flow in the tubes, and (3) model the effect of fins on heat transfer and pressure drop using a PMM. It is expected that the PMM will allow for accurate capture of enhanced heat transfer between the exhaust gas and the steam-filled tubes without resolving the small geometric features such as fins. This approach should maintain the mesh element counts within a reasonable limit. Moreover, the accurate flow and heat transfer data generated from high-fidelity simulations based on the PMM will facilitate the search of optimum design and operating conditions for HRSGs compared to the approximate PM approach.

2. BENEFITS OF FUNDING DOE OFFICE'S MISSION

The Fossil Energy & Carbon Management Program Office (FECM) in the U.S. Department of Energy funded this collaboration through the High-Performance Computing for Materials (HPC4mtls) program. The underlying objective of the program is to address key challenges in developing, modifying, and/or qualifying new or modified materials that perform well in severe or complex environments through the application of HPC, modeling, simulation, and data analysis. Industry participants benefit from a combination of multiphysics computational tools executed to maximize the strengths of each tool on HPC resources hosted at DOE's national laboratories. These efforts will provide a thorough understanding of multiphysics phenomena in manufacturing operations and will inform possible improvements to crucial process parameters.

In support of DOE's mission to grow the American economy, implement process development, and enhance the energy efficiency of manufacturing operations, this collaboration between the Electric Power Research Institute (EPRI) and Oak Ridge National Laboratory (ORNL) accomplished the following objectives using ORNL's HPC resources:

- Established a methodical flow of process information and geometric details from EPRI to ORNL pertinent to the Heat Recovery Steam Generator engineered by Vogt Power, Inc.
- Developed and validated a CFD model capable of estimating the oxide thickness inside of high-temperature HRSG HX tubes on a reduced scale HX model
- Developed a strategy to approximate the effect of HX tube fins on the heat transfer in the HRSG tubes, which is otherwise computationally very expensive to capture in the simulation
- Acquired high-fidelity flow and temperature data in the vicinity of the tubes to better understand the heat transfer from the exhaust gas to the steam in the tubes
- Acquired oxidation maps from simulations in different HRSG HX sections

This effort advances the conventional understanding of flow and heat transfer–induced oxidation in the HRSG HX tubes at a scale of detail that can be provided by HPC resources. This level of detail is impractical to obtain through physical field tests. The methodology developed and the results obtained during this project will help optimize the design of current and future HRSGs to minimize oxidation growth and subsequent exfoliation, thus reducing maintenance costs.

3. TECHNICAL DISCUSSION OF WORK PERFORMED BY ALL PARTIES

3.1 PRELIMINARY CFD MODEL DEVELOPMENT, VERIFICATION, AND PREDICTIONS

This section discusses the details of the CFD model to be used for simulation of a plant-scale or real-scale HRSG to study the oxidation. The oxidation model was verified with the analytical model data from Sabau and Wright (Sabau & Wright, 2009), and the CFD model was verified and validated with the fin heat transfer simulation (Lindell, 2019) and experimental investigations (Ward, 1958). The validated CFD model was used to simulate and study the oxide thickness differences between bare and finned tubes to determine the effect of fin heat transfer on the accuracy of oxide thickness. The technical content discussed in this section is from Panicker et al. (Panicker, Delchini, Sambor, Sabau, & Jain, 2021).

3.1.1 Oxidation Model

The oxidation process in HRSGs involves complex physical and chemical phenomena that cannot be fully resolved because of the wide range of spatial and temporal scales and because of the lack of a well-established theory. This theoretical gap is commonly addressed using macroscopic models to capture the microstructural features while maintaining physical accuracy. The oxidation model proposed by Sabau and Wright (Sabau & Wright, 2009) was chosen to model the oxide growth on the steam-side tubes of the HRSGs. This model is based on the parabolic oxidation relationship, as

$$d^2_{ox,(k)} = d^2_{ox,(k-1)} + d\left(d^2_{ox}\right), \tag{1}$$

where $d(d_{ox}^2) = 2\ \Delta t\ k_p[\ T_{gr}(t_k)\ ]$ is the incremental amount of oxide grown on the tube wall between times t_{k-1} and t_k. The temperature T_{gr} denotes the temperature at the interface between the steam and the oxide/wall, or oxide growth temperature. The parabolic rate constant k_p is defined as $k_p(T) = Ae^{-Q/RT}$, where A is the Arrhenius constant, Q is the activation energy for the rate-controlling process, R is the universal gas constant, and $T = T_{gr}$ is the oxide growth temperature. The oxidation process described in Eq. (1) is controlled by the oxide growth temperature T_{gr} that is commonly assumed to be equal to the steam temperature for simplicity. A more advanced approach accounts for the thermal boundary layer between the steam and the oxide, which causes T_{gr} to be higher than the mean steam temperature. Under such an assumption, the oxide growth temperature can be computed using an iterative process by solving the temperature equation coupled to Eq. (1). See Section A and Table II of Sabau and Wright (Sabau & Wright, 2009) for further details. This approach yields a better prediction of the oxide thickness for both partial- and full-load regimes (Sabau & Wright, 2009).

The oxidation model described by Sabau and Wright (Sabau & Wright, 2009) was implemented in the CFD commercial package STAR-CCM+ by adding a shell to the boundary between the inner face of the tube and the steam. The temperature field between the shell and the boundary face was mapped to compute the oxidation thickness and the thermal resistance to be added after each time step. Note that in this model, the oxide growth does not affect the geometry of the inner tube; it only adds a thermal resistance that is proportional to the oxide thickness and the oxide thermal conductivity ($k_{ox} = 3.0\ W\,/\,m$ - K). The implementation was then tested for full- and partial-load regimes using the same oxidation parameters as those used in Section A of Sabau and Wright (Sabau & Wright, 2009). The numerical solution was then compared to the analytical solution obtained for a simple one-dimensional case as given in Section A of Sabau and Wright (Sabau & Wright, 2009). The numerical results presented in Figure 1 show a very good agreement with the analytical solution; these results were obtained using a second-order spatial and temporal scheme.

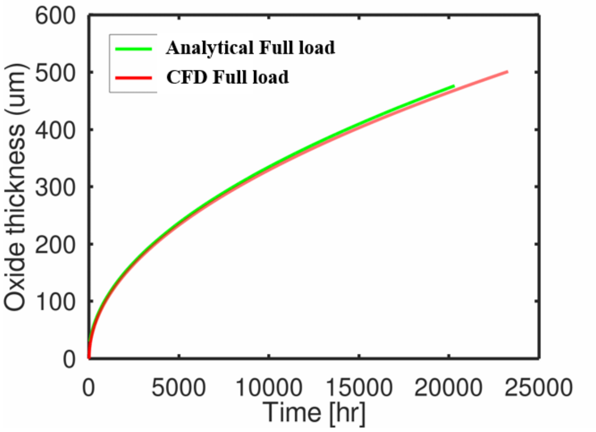

Figure 1. Comparison of oxide evolution for full load: STAR-CCM+ vs. analytical solution.

A mesh convergence study was also performed to demonstrate the correct implementation of the oxidation model in STAR-CCM+. The grid convergence indices (GCIs) are reported in Table 1 for the oxide thickness, along with uncertainty and error estimates with respect to the best estimate (463.39 μm). Error estimate, uncertainty, and best estimate were computed using the method described in Eca and Hoekstra (Eca & Hoekstra, 2014). It was also determined that a second-order accuracy is achieved for this test, with a standard deviation of 0.79.

Table 1. Convergence grid indices for the oxide thickness

Mesh size (mm)	Oxidation thickness (μm)	GCI	Error estimate	Uncertainty
10.0	442.10	-	-20.63	47.87
5.0	406.93	6.1E-03	-5.15	9.70
2.5	461.91	3.2E-04	-1.28	3.89
1.25	462.28	1.21E-04	-5.15	2.31
0.625	462.24	1.31E-05	-0.08	2.04

Results presented in Table 1 show that the solution is converged for a grid size lower than or equal to 2.5 mm. The best estimate value achieves a relative error of 1.3% with respect to the solution obtained from the oxidation model (469.65 μm), which is an acceptable error for our application and confirms the successful implementation of the model in STAR-CCM+. Implementation of the oxidation model in STAR-CCM+ will be used with the CFD model of the HSRG described in Section 3 to predict oxidation thickness.

3.1.2 Computational Fluid Dynamics Model of an HRSG

The HRSG at the real scale (~10 - 50 m) consists of multiple sets of compact HXs that extract and reuse heat from the gas turbine's incumbent exhaust gas. The tubes in the HX unit are wrapped with thin fin structures to enhance their ability to extract more heat. Capturing such thin structures with a computer-aided design (CAD) package for a real-scale HRSG and simulating the process using a CFD model is not computationally feasible, aside from introducing complexity at the simulation setup. However, capturing the effect of such structures in exchanging heat in the simulation cannot be excluded, especially for predicting accurate oxide thickness in the tubes.

A CFD model accounting for the flow, thermal, and oxide growth physics in an HRSG was verified and validated based on the fin heat transfer simulation (Lindell, 2019) and experimental investigations (Ward, 1958). Various comparisons of heat transfer, pressure drop, and oxide thickness for a small section of tubes were performed with and without fins and are presented in the subsequent subsections. The comparisons show that the need to model the effect of fins on the real-scale HRSG is crucial for the accurate prediction of oxide thickness.

3.1.2.1 Geometry and simulation description

The geometry considered here is a 3D rectangular channel with 6 rows of finned tubes. As shown in Figure 2 (left), the hot gas or air enters the rectangular channel at the inlet, passes through the tube rows, and exits at the channel outlet. Gas passing through the tube rows results in heat transfer from the tubes to the gas. Note that the heat transfer from the steam flowing inside the tubes to the walls of the tubes is modeled with a convective boundary by specifying the heat transfer coefficient and the steam temperature as given by Lindell (Lindell, 2019). The flow and thermal properties of air and the copper tubes used in the study can also be found in Lindell (Lindell, 2019). The surface-averaged outlet temperature of the hot gas and the pressure drop across the channel are monitored in the simulation until a steady value is reached, and then it is compared with the experimental data. All simulations were run on 48 central processing units with a second-order numerical scheme and a steady-state solver, resulting in a runtime of 2–3 hours to reach convergence.

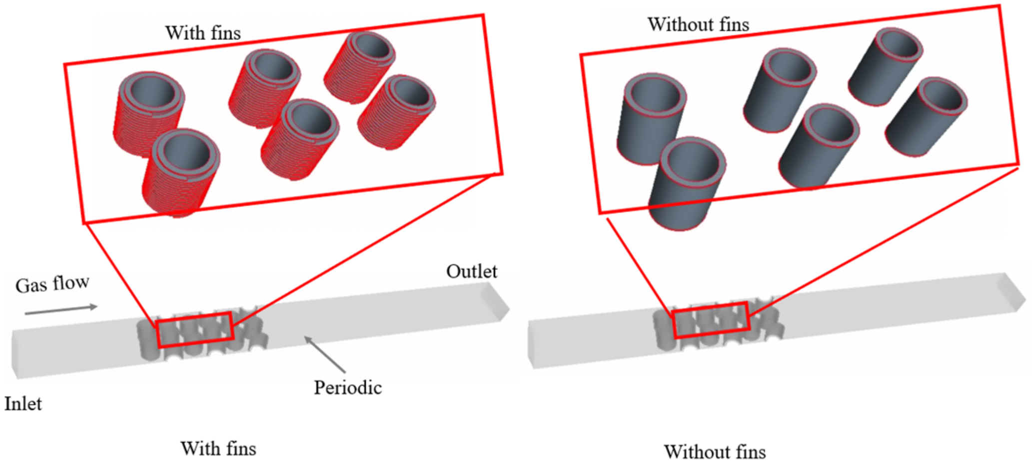

Figure 2. CAD model with fins (left) and without fins (right).

3.1.2.2 Mesh convergence, numerical schemes, and validation

The mesh convergence study was performed on five different mesh sizes ranging from 10 to 54 million cells to analyze the numerical error involved in the spatial schemes selected for the study. The STAR-CCM+ trimmed cell mesher was used to generate hexahedral cells as shown in the section plane in Figure 3. A base mesh size of 12 mm was used to route the flow away from the tubes; cylindrical refinement boxes were created around each tube to refine the mesh around the fins and tubes. A mesh size of approximately 0.4 mm was used to refine the mesh with 54 million cells. Two prism layers were added on the boundary walls to achieve a wall Y^+ value below 1, conforming with the Y+ value used in (Lindell, 2019). The shear stress transport (SST) k-Omega turbulence model was used, along with a second-order accurate steady-state solver. Variations of the pressure drop, the surface-averaged outlet temperature, and the residual norms (all below 10^{-4}) were monitored to detect convergence to a steady-state solution.

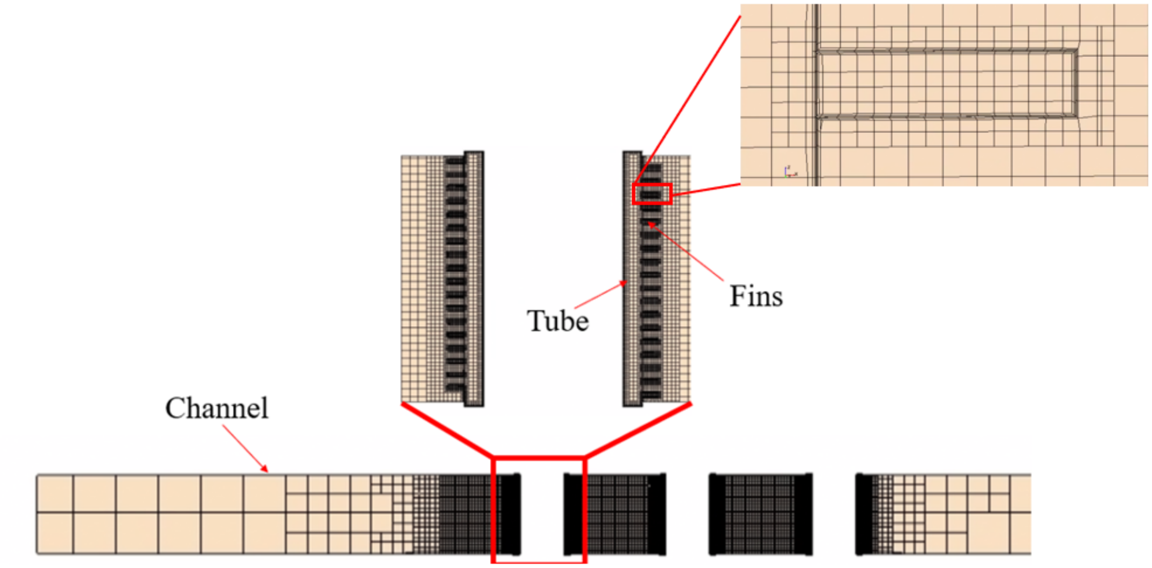

Figure 3. Mesh on a cut plane.

The pressure drop across the channel and the average outlet temperature obtained from the simulations for these meshes are presented in Figure 4 and shown in Table 1. The convergence order and best-estimate values were computed with the least-square fit introduced by Eça and Hoekstra (Eca & Hoekstra, 2014). It was found that the convergence parameters for the pressure drop and temperature had convergence orders of 1 and 1.5, best estimates of 493 Pa and 348.72 K, and standard deviations of 4.76 Pa and 1.4 K, respectively. Note that the error estimate represents the error between the CFD value and the best estimate. The uncertainty informs the confidence interval that contains the exact solution with 95% coverage. As shown in the plots, the surface-averaged outlet temperature reached a plateau after a mesh count of approximately 16 million cells; however, the pressure drop converged within 5% relative to the most refined mesh at a mesh count of approximately 24 million cells.

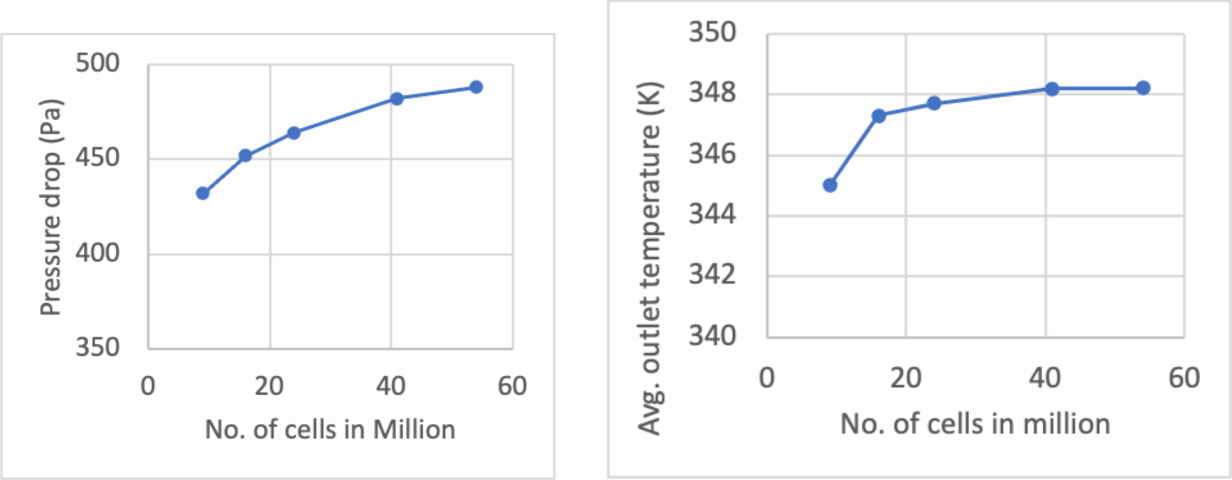

Figure 4. Mesh on a vertical plane perpendicular to the gas flow cutting the tubes.

The pressure drop, outlet temperature, and averaged heat transfer coefficient of the tubes predicted by the CFD model for the most refined mesh and from the experimental investigation (Ward, 1958) are reported in Table 2. The comparisons between experimental and CFD results from the most refined mesh show that the errors were below 5% for all quantities compared. The second-order accuracy was not recovered, but this type of behavior is common for multiphysics models with strong nonlinear effects. The best-estimate values were within a few percentages of the experimental values, which demonstrates the accuracy of the model while results in Figure 4 are evidence that the asymptotic range was reached.

Table 2. Comparison of quantities obtained from the CFD simulation of fins vs. the experiment (Ward, 1958)

Quantities	CFD result	Experiment	Relative error	Convergence order	Best estimate
Pressure drop (Pa)	491	510	3.8 %	1	493
Average outlet temperature (K)	348	346	0.5 %	1.5	348.72
Average heat transfer coefficient for all tubes (W/m^{2}K)	128	130	1.5 %	–	–

3.1.2.3 Flow and temperature profile comparison with fin and without fin

This section compares the numerical results obtained with a geometry in which the fins were directly modeled (with-fin) and a geometry in which the fins were not directly modeled (without-fin). The objective is to quantify the effect of the fins on flow parameters using the CFD model described in Section 3.2. Figure 5 presents the temperature profiles on a plane section parallel to the flow for the models with and without fins. It can be observed that the gas passing through the tubes with fins was hotter than that passing through tubes without fins. This is due to the enhanced surface area for heating provided by the fins. Furthermore, the heat transfer between the tubes and the gas going through the channel are controlled mainly by the surface area of the tubes, as well as the turbulence in the flow. Figure 6 presents the velocity profiles on the same plane section for geometries with and without fins. It can be observed that the maximum velocity in the case with fins was higher than in the case without fins; this is due to the gas flow passing through the narrow passages between the fins. The pressure drop across the channel obtained from the CFD study for the case with fins was 485 Pa, whereas for the case without fins, it was 240 Pa. The values indicate that there was a difference in pressure drop between the with-fin and without-fin cases. Therefore, when modeling the effect of fins on heat transfer for the real-scale HRSG, the effect of pressure drop must also be considered.

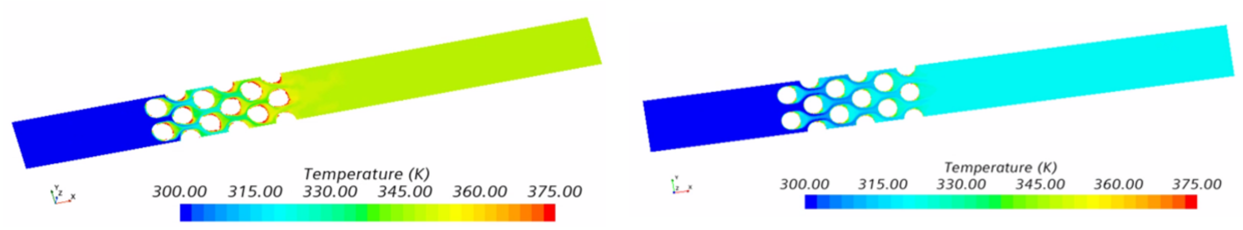

Figure 5. Temperature on a cut section plane parallel to the flow with fins (left) and without fins (right).

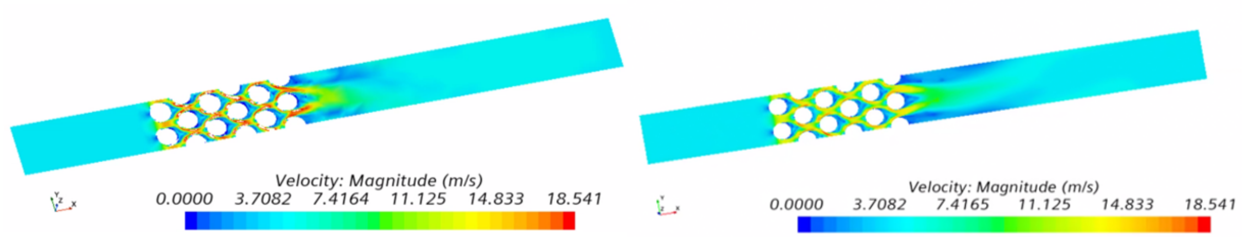

Figure 6. Velocity on a cut section plane parallel to the flow with fins (left) and without fins (right).

The numerical results shown in Figure 5 and Figure 6 demonstrate the need to model the effect of the fins on the heat transfer and the pressure drop. This is particularly important for heat transfer, as the oxide growth is mainly a temperature-driven physical phenomenon, so it is sensitive to heat transfer between steam and gas, as detailed in Section 3.1.3.

3.1.3 Prediction of the oxide thickness for with-fin and without-fin cases using realistic thermal conditions for the HRSG

In this section, the sensitivity of the oxide thickness on the steam-side of the tubes to the enhanced heat transfer caused by the fins is investigated. The oxidation model presented in Section 3.1.1 is merged with the CFD model from Section 3.2 to predict the oxide thickness on the steam side of the tubes. The growth of the oxide layer is typically observed for very high temperatures (700–900 K) that are encountered in the HRSG. Therefore, CFD simulations to predict oxide thickness were conducted by changing the inlet gas temperature to 883 K and the temperature in the tubes to 751 K so that the heat transfer was from the gas to the tubes and the steam, as observed in the real-scale HRSG. Two different inlet gas velocities of 4 and 16 m/s were considered when comparing oxide thicknesses in tubes with and without fins. A second-order spatial and temporal integrator was used in this study. The flow solution was first developed using a steady solver before switching to an unsteady solver and turning the oxidation model on to predict the oxide growth over 10 years. The oxide thickness contour comparison between with-fin and without-fin cases for individual tubes at an inlet gas velocity of 4 m/s is reported in Figure 7. The contour plots show a significant difference in the local values of oxide thicknesses with and without fins. It is important to note that the tubes in rows 1 and 2 show a higher oxide layer thickness for the finned tubes. On the contrary, for the finless tube case, the tubes in rows 4, 5, and 6 show the maximum oxide layer growth. The oxide thickness contours for an inlet gas velocity of 16 m/s are reported in Figure 8: the trend of oxide thickness contour observed for an inlet gas velocity of 16 m/s remains the same as the case with an inlet gas of velocity 4 m/s, with the higher oxide thickness for 16 m/s cases. In both cases, the oxide thickness is higher with fins than without fins: more heat is being transferred to the steam in the with-fin case, yielding a higher temperature of the inner wall and consequently a faster oxide growth per Eq. (1). This phenomenon is further enhanced by the low thermal conductivity of the oxide that acts as an additional thermal resistance. Moreover, the difference in oxide thickness with and without fins is more prominent at the higher inlet gas velocity of 16 m/s. This is explained by the higher enthalpy rate and the increased turbulent mixing for the high inlet velocity (16 m/s) than for the low inlet velocity (4 m/s), thus leading to more heat being transferred in the former case.

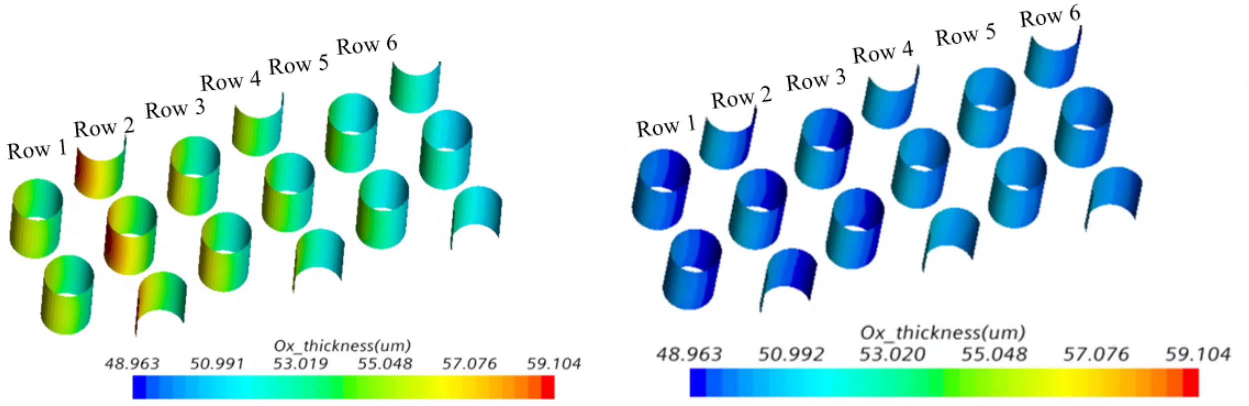

Figure 7. Oxide thickness Ugas = 4 m/s with fins (left) and without fins (right).

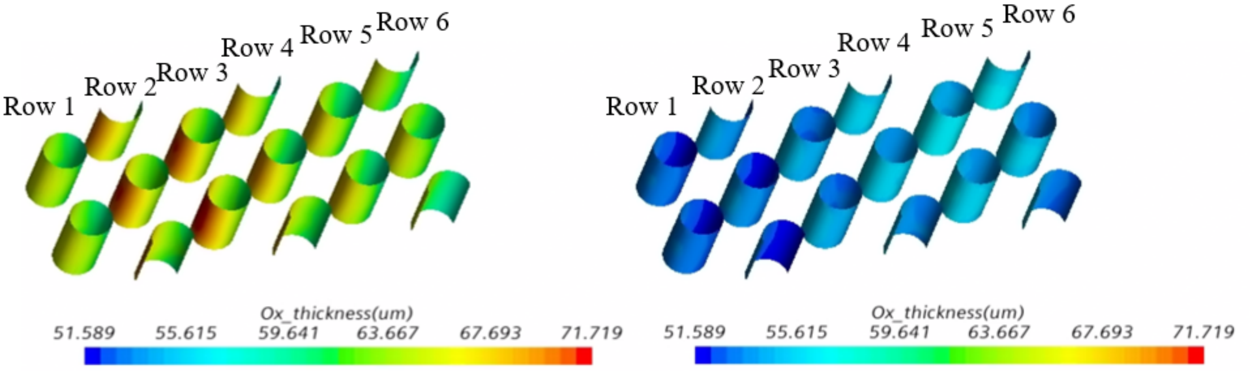

Figure 8. Oxide thickness Ugas = 16 m/s with fins (left) and without fins (right).

Figure 9 shows the surface-averaged oxide thickness growth predicted by the CFD model for inlet gas velocities of 4 and 16 m/s over a period of 10 years. The results indicate that the difference in averaged oxide thickness growth is greatest for the high inlet gas velocity of 16 m/s, further reiterating the need to model the effects of fins on the oxide thickness for a real-scale HRSG.

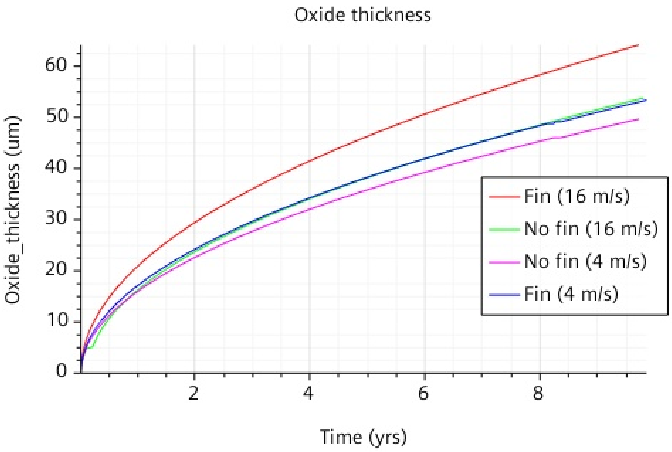

Figure 9. Average oxide thickness on all the tubes with and without fins for different inlet gas velocities over multiple years.

3.2 MODELING THE EFFECT OF THE FINS ON THE HEAT TRANSFER AND PRESSURE DROP USING A POROUS MEDIA MODEL

This section demonstrates that the PMM can be used to model the effect of fins on heat transfer and pressure drop. If successful, this approach would considerably reduce the meshing constraints that are mostly driven by the small geometric fins in HRSGs. Accurately modeling flow path and heat transfer between the hot gas and the fins requires a very fine mesh near the fins, which increases the mesh size and the runtime. The fin region is defined as the region surrounding each HRSG tube that is of the same thickness and same height as the fins. Because of its non-regular geometry, the fin region includes both the gas phase and the fin, so the region is treated as a mixture of gas and solid phases, as shown in Figure 10.

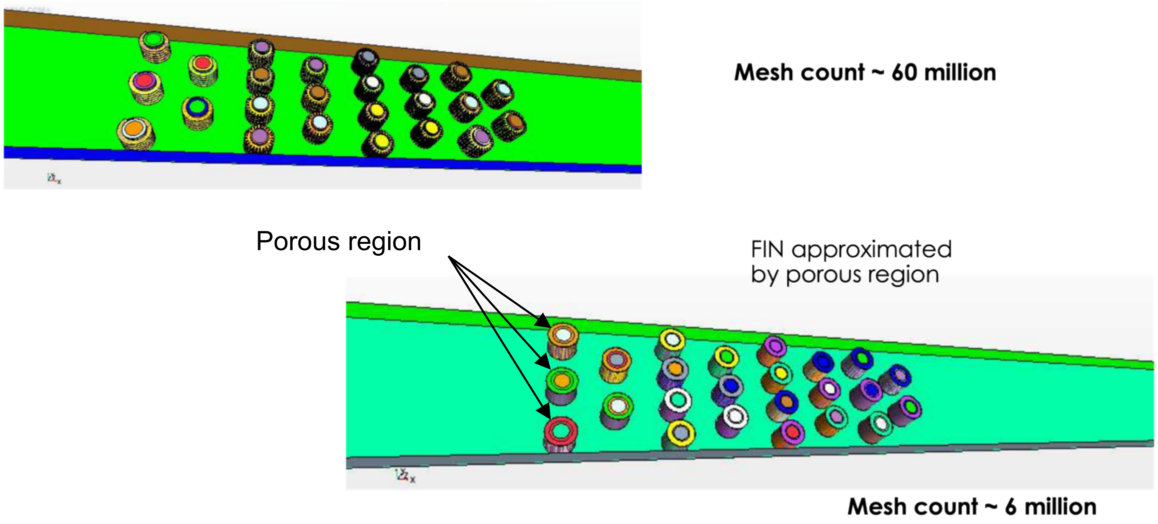

Figure 10. CAD model showing how the fin regions are approximated by a porous region.

3.2.1 The Porous Media Model

The PMM implemented in STAR-CMM+ relies on the physical velocity formulation that accounts for the increase in velocity when the flow enters the porous medium. The continuity equation, the momentum equation, and the energy equation are expressed as a function of mixture quantities weighted by the porosity and function of the thermodynamic properties of the liquid and solid phases. Reynolds-averaged Navier-Stokes (RANS) models are available to model turbulent flows. A description of the equations implemented in STAR-CCM+ and the applicability of the PMM to non-Darcy flow can be found in the Siemens STAR-CCM+ manual (Siemens Digital Industries Software, 2021).

3.2.2 Modeling of Pressure Drop and Heat Transfer Using the Porous Media Model

The PMM implements a set of source terms referred to as *Forchheimer source terms* that are commonly used to model pressure drops. These source terms are controlled by two independent coefficients that can be tuned to match reference pressure drops over a range of inlet velocities. The enhanced heat transfer from the fins between the gas and the steam flowing inside the pipes is modeled by tuning the porosity and the solid thermal conductivity parameters. Note that there are no dedicated source terms for modeling heat transfer in the PMM. In the remainder of this report, the parameters to model the pressure drop are referred to as *Forchheimer parameters*, and the parameters to model heat transfer are referred to as *heat transfer parameters*.

The effect of the fins on the pressure drop and the heat transfer are a function of the fin types and their characteristics. Therefore, there are different Forchheimer and heat transfer parameters for different fin types. For simplicity, it is assumed that the parameters will be constant for each fin type.

3.2.3 Procedure to Optimize the Forchheimer and the Heat Transfer Parameters

The Dakota optimization package (Adams, November 2021) was used to optimize the Forchheimer and heat transfer parameters with a non-linear least square method (nl2sol). Global and local methods were both investigated and yielded similar results. The pressure drop and the gas outlet temperature were defined as reference values. The optimization method was run with four different inlet velocity values ranging from 4 m/s to 32 m/s and an inlet temperature of 883.0 K. The Forchheimer parameters were assumed positive in the study. In this study, the porosity and thermal heat conductivity of the PMM (heat transfer parameters) were constrained by the physical values. The porosity was set to vary between 0.0 and the physical porosity computed from the geometry characteristics (volume of gas / (volume of gas phase + volume of fin)). The thermal heat conductivity was bounded by the thermal conductivity of the gas phase and the fin material. Dakota is integrated to the Nuclear Energy Advanced Modeling and Simulation (NEAMS) Workbench, which is a user-friendly graphical user interface (GUI) (Delchini, Swiler, & Lefebvre, 2021). The NEAMS Workbench was used as the front end to drive Dakota, which in turn drives the STAR-CCM+ input deck described in Section 3.1. The optimization process was run on the ORNL HPC platform Ridge. A Dakota input file was edited with the appropriate variables, their lower and upper bounds, and the optimization method (nl2sol). After executing Dakota, sub-working directories were created on the ORNL HPC platform containing an optimization that was run for a given set of Forchheimer parameters and heat transfer parameters supplied by the Dakota optimization method. Once the optimization run was deemed converged, the pressure drops and the gas temperature at the outlet boundary were extracted using a Java script. These values were then returned to the Dakota optimization method, which generated a new set of parameters. This optimization process can be time consuming, so the initial values must be chosen carefully to minimize the number of optimization runs. Once the optimization process was complete, the STAR-CCM+ input deck with the optimized parameters was run to check the flow patterns, physics, pressure drop, and gas outlet temperature. The optimization process was performed independently for each section of the HRSG relevant to this project (HPSH1, HPSH2, RHTR1 and RHTR2).

3.2.4 Numerical Results from the Porous Media Model

This section presents results obtained from using the PMM in STAR-CCM+ for four sections of the HRSG+: high-pressure superheater (HPSH)1, HPSH2, reheater (RHTR)1 and RHTR2. The CFD model that is presented, verified, and validated in Section 3.1 was used to generate reference values for each section listed above and is referred to as *with-fin CFD model* in subsequent sections. Results are reported in Table 3 through Table 6 for all aforementioned sections of the HRSG.

Table 3. Comparison of pressure drops and heat transfer between the with-fin CFD model and the PMM for the HPSH1

Inlet velocity	With-fin pressure	With-fin temperature	PMM pressure	PMM temperature
4.0	8.34	869.07	8.099	870.61
8.0	28.0	872.72	26.92	873.62
16.0	93.4	875.8	89.76	876.20
32.0	300.0	878.68	301.9	878.77

Table 4. Comparison of pressure drops and heat transfer between the with-fin CFD model and the PMM for the HPSH2

Inlet velocity	With-fin pressure	With-fin temperature	PMM pressure	PMM temperature
4.0	22.9	852.68	22.87	852.78
8.0	75.78	861.93	71.57	862.69
16.0	252.6	869.55	237.58	869.74
32.0	828.0	876.10	825.11	875.76

Table 5. Comparison of pressure drop and heat transfer between the with-fin CFD model and the PMM for the RHSH1

Inlet velocity	With-fin pressure	With-fin temperature	PMM pressure	PMM temperature
4.0	22.69	848.39	22.66	848.94
8.0	73.57	859.73	72.51	859.98
16.0	249.78	868.61	243.87	867.90
32.0	861.73	875.7	852.08	874.79

Table 6. Comparison of pressure drops and heat transfer between the with-fin CFD model and the PMM for the RHSH2

Inlet velocity	With-fin pressure	With-fin temperature	PMM pressure	PMM temperature
4.0	36.46	836.83	36.52	837.17
8.0	114.42	852.20	110.25	853.22
16.0	373.08	864.42	357.87	864.87
32.0	1238	874.32	1235.7	874.15

The pressure drops and gas outlet temperatures predicted by the PMM are in good agreement with the reference values for all inlet conditions. The relative error is below 5% for all sections. The Forchheimer source terms were calibrated to model the pressure drops induced by the fins on the gas flow. The porosity and the thermal conductivity of the solid phase were calibrated to model the enhanced heat transfer from the fins and thus to extract the correct amount of heat from the hot gas.

For completeness, comparison between the velocity profile and the temperature profile are presented for the geometry used in Section 3.1 to verify and to validate the CFD model (15, referred to as the *with-fin model*). An equivalent PMM input deck was created with STAR-CCM+. After calibrating the Forchheimer and heat transfer parameters, results between the with-fin model and the PMM were compared. Figure 11 and Figure 12 show the velocity profile in the gas phase predicted by the with-fin model and the PMM, respectively. Both models display the same variations and the similar extremum values. The with-fin model was run with a finer mesh to resolve the flow around the fins as opposed to the PMM, which models the fins and thus can be run with a coarse mesh. Figure 13 and Figure 14 show the temperature profile in the gas phase obtained using the with-fin model and the PMM. Again, it can be observed that both models display similar variation and extremum values. The temperature profile on the inner surface of the pipes is reported in Figure 15 and Figure 16 for the with-fin model and the PMM, respectively. It can be seen that both models have similar variations.

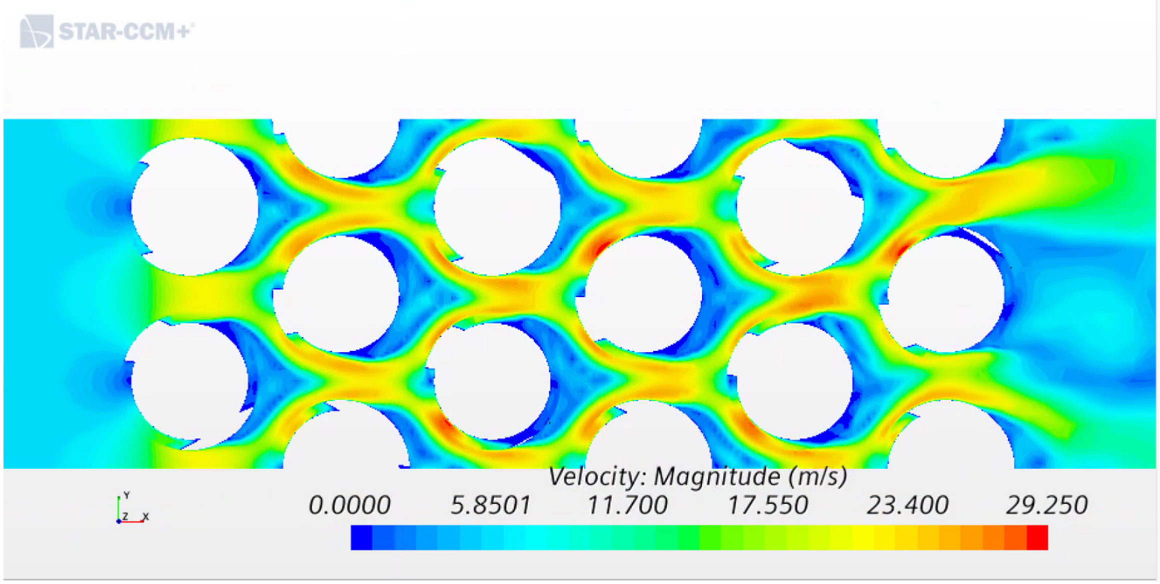

Figure 11. Gas velocity profile obtained using with-fin model.

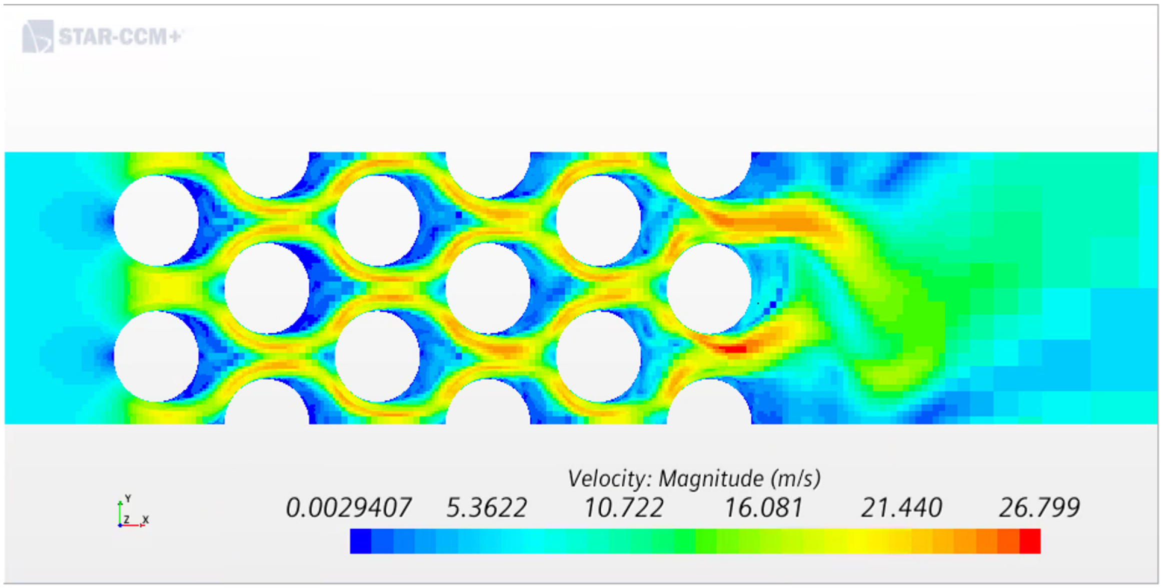

Figure 12. Gas velocity profile obtained using PMM.

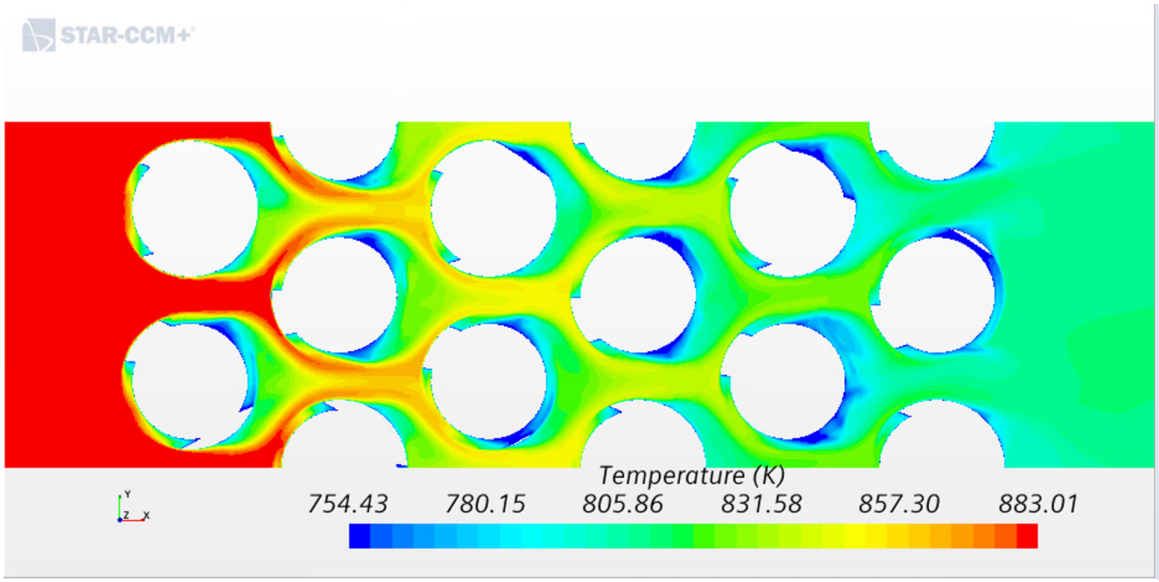

Figure 13. Gas temperature profile obtained using the with-fin model.

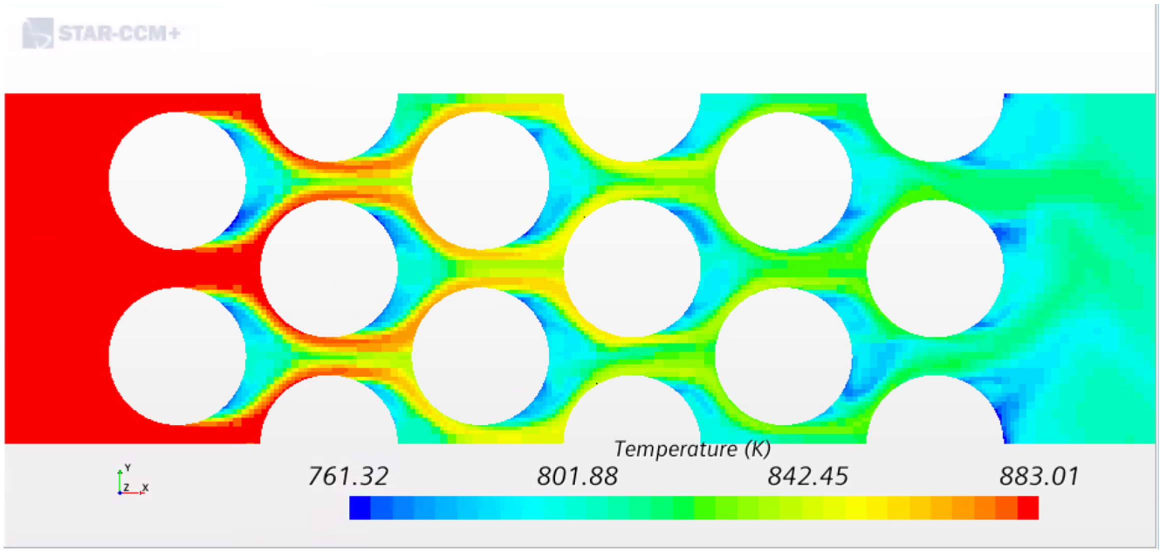

Figure 14. Gas temperature profile obtained using PMM.

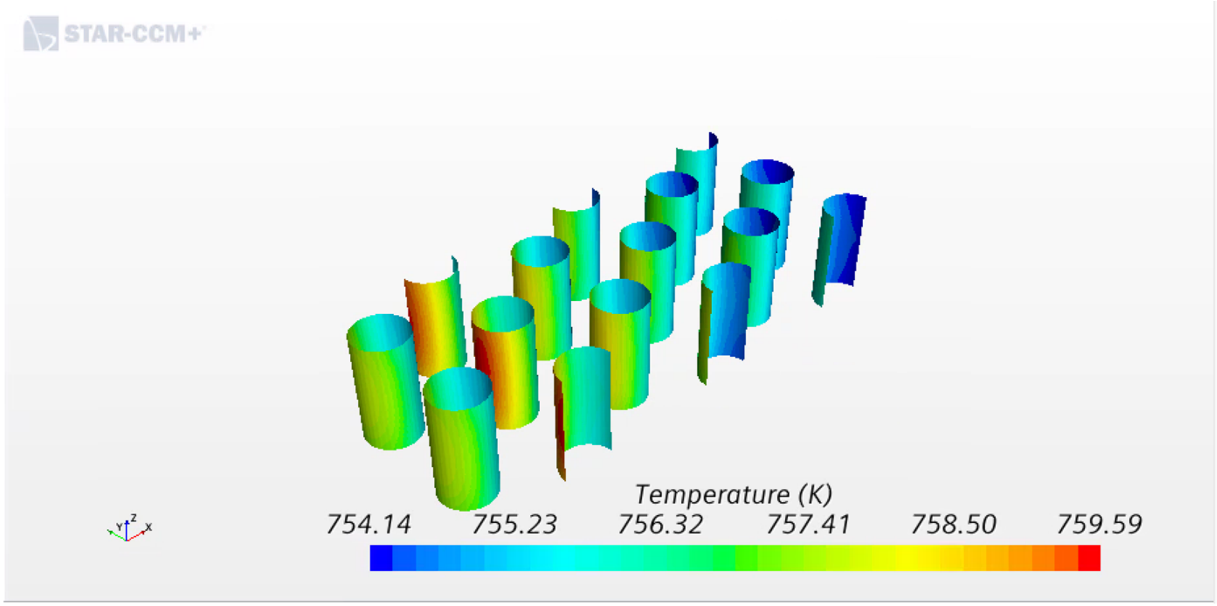

Figure 15. Temperature profile of the inner surface pipes obtained using with-fin model.

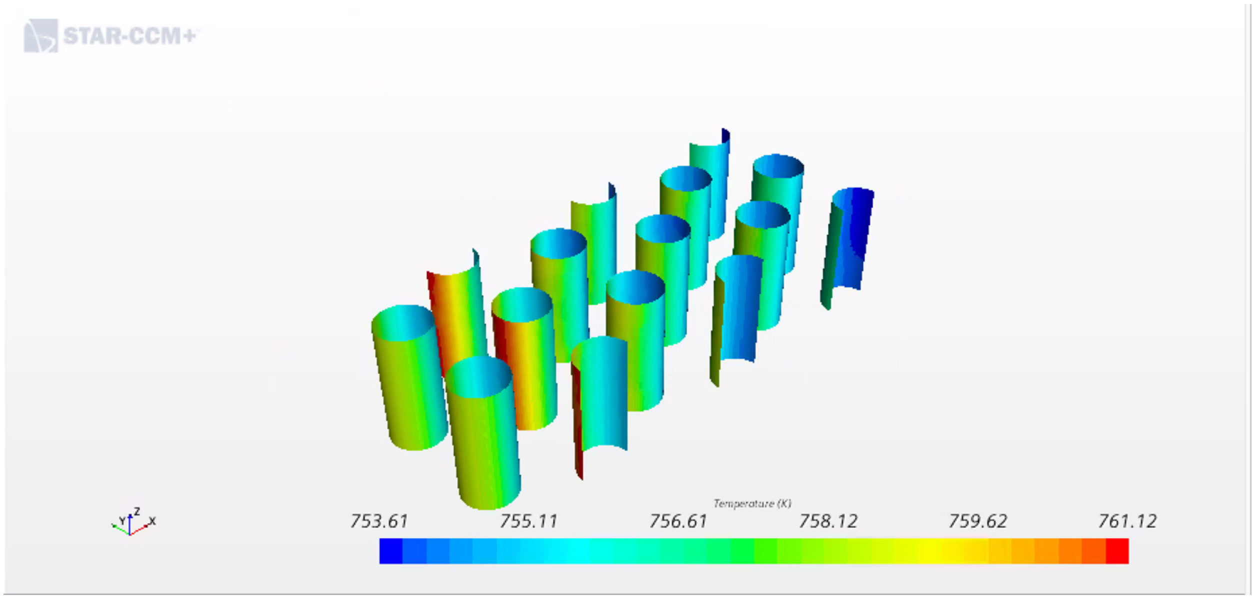

Figure 16. Temperature profile of the inner surface pipes obtained using PMM.

The results presented in Figure 11 through Figure 16 demonstrate that the PMM can effectively and accurately model the effect of the fins on the pressure drop and the heat transfer. The gas velocity and gas temperature profiles have similar variations. The same conclusion can be drawn for the temperature profile on the inner surfaces of the pipes. Remembering that the oxidation model implemented in Section 3.1 is temperature driven, it can be concluded that the PMM should be able to predict the oxide thickness on the inner surface of the pipe while avoiding the mesh constraints caused by the small geometric features present in the fins.

3.2.5 Comments on the PMM Approach

The PMM approach presented in this section calls for a few comments:

- The calibration study was performed using an incompressible CFD model which in theory means the Forchheimer parameters for the pressure drop from the heat transfer parameters are decoupled. The incompressible assumption could have made the optimization process easier because the pressure effect and thermal effects are decoupled: the Forchheimer parameters could be calibrated first, and then the heat transfer parameters are calibrated. If the density depends on temperature or if the flow is compressible, then this process will no longer work.

- The Forchheimer source terms and the solid thermal conductivity can be set as scalar, diagonal tensor, or full tensor. In the calibration study presented in this section, each calibration parameter was set to a scalar. The same calibration study could be performed with tensors, which would lead to additional parameters to calibrate and would provide additional degree of freedom to potentially capture more complex phenomena. Setting the Forchheimer source terms and the solid thermal conductivity to scalar entries in the CFD input deck provided a sufficient degree of freedom to capture the physics to model in this project.

- The current PMM approach does not investigate how varying the inlet temperature affects the Forchheimer and heat transfer parameters. Such a study would be required to run transients of an HRSG, in addition to the range of inlet velocities already investigated.

- The calibration of the Forchheimer and heat transfer parameters depend on the mesh size. The reference values should be obtained from a converged CFD solution to minimize the effect of the discretization and the mesh. A convergence study of the PMM is also recommended to ensure that the mesh will capture the physics for modeling. Note that performing a calibration study with an under-resolved mesh would still work, but it would yield parameter values that would not be valid when refining the mesh.

- Calibration of the Forchheimer and heat transfer parameters require reference values that can vary based on the data available. For instance, the outlet temperature of the steam pipe could be used to calibrate the heat transfer parameters instead of the gas outlet temperature. The outlet temperature of the steam pipes is commonly available in HRSGs. In the calibration study presented in this section, the outlet temperature of the gas was chosen as a reference value because it varies significantly between inlet conditions.

- It is worth noting that the PMM approach can effectively and accurately resolve the effect of the fins on the heat transfer and the pressure drop with a mesh that is about 10 times smaller than that used for the with-fin model. This will be of particular importance when modeling larger geometries with hundreds of steam pipes, as will be demonstrated in Section 3.3.

3.3 REYNOLDS-AVERAGED NAVIER-STOKES SIMULATION OF THE REAL-SCALE HRSG AND OXIDE THICKNESS PREDICTION

3.3.1 Computational Fluid Dynamics Model

Exhaust gas flow in the duct and steam flow in the HX tubes are assumed to be incompressible (the flow is low-Mach, and variations of the thermo-physical properties remain small with respect to the temperature range). Thermo-physical properties (refer to Table 7) are evaluated at the operating pressures and temperatures of the duct and the different HX sections. Note that thermo-physical properties for air were used rather than for exhaust gas due to their relatively similar chemical composition and heat transfer properties (e.g. specific heat), as well as the fact that properties of air are readily available. The inlet flow conditions used for the tubes and the duct are summarized in Table 8. STAR-CCM+ (commercial CFD code) was used to generate the mesh and to conduct the simulations. A realizable k-epsilon model with a wall function that is valid for all ranges of wall Y+ was used to capture the turbulent flow and turbulent heat transfer from the exhaust gas to the tubes. Note that the turbulence model used in the section vary from the model used for PMM development because the wall resolution used for PMM was very high (Y+ ~ 1), since those resolutions are not achievable in the full-scale geometry due to high computational cost while realizable k-epsilon is used in many full-scale applications at lower wall resolution (Y+>30) to successfully predict turbulence, than the turbulence model used in PMM, the realizable k-epsilon model was selected for the simulation of the full-scale HRSG. An uncertainty in the pressure drop prediction is expected due to the change in turbulence models, however, it is assumed to be small. The equations governing the exhaust gas/steam flow and heat transfer, along with their constitutive relations, are shown below. Flow and heat transfer inside the system is allowed to reach a steady state first, then the oxidation model is introduced, and then a transient flow and heat transfer solver is used.

Continuity

$$\frac{\partial \rho_\phi}{\partial t} + \nabla \cdot \rho_\phi u_\phi = 0 \tag{1}$$

Momentum

$$\frac{\partial \rho_\phi u_\phi}{\partial t} + \nabla \cdot \rho_\phi u_\phi u_\phi = -\nabla p_\phi + \nabla \cdot \boldsymbol{\tau}_\phi + \rho_\phi \boldsymbol{g} \tag{2}$$

Energy

$$\frac{\partial \rho_\phi C_{p\phi} \alpha_\phi T_\phi}{\partial t} + \nabla \cdot \rho_\phi C_{p\phi} u_\phi T_\phi = \nabla \cdot \alpha_\phi k_{\phi\mathrm{eff}} \nabla T_\phi \tag{3}$$

Turbulence

$$\frac{\partial \alpha_\phi k_\phi}{\partial t} + \nabla \cdot \alpha_\phi u_\phi k_\phi = \nabla \cdot \nu_{\mathrm{eff},\,\phi} \nabla k_\phi + P - \varepsilon \tag{4}$$

$$\frac{\partial \alpha_\phi \varepsilon_\phi}{\partial t} + \nabla \cdot \alpha_\phi u_\phi \varepsilon_\phi = \nabla \cdot \nu_{\mathrm{eff},\,\phi} \nabla \varepsilon_\phi + C_{1\varepsilon} \frac{\varepsilon_\phi}{k_\phi} P - C_{2\varepsilon} \frac{{\varepsilon_\phi}^2}{k_\phi} \tag{5}$$

where, φ= air, steam,

$$\nu_{\mathrm{eff}} = \nu_{\mathrm{lam}} + \nu_{\mathrm{T}}\,,\ \nu_{\mathrm{T}} = C_\mu \frac{{k_\phi}^2}{\varepsilon_\phi}\,,\ C_\mu = 0.09,\ C_{1\varepsilon} = 1.44,\ C_{2\varepsilon} = 1.92, \tag{6}$$

$$\boldsymbol{\tau}_\phi = \alpha_\phi \mu_{\phi\mathrm{eff}} \left[\nabla u_\phi + \left(\nabla u_\phi\right)^T - \tfrac{2}{3}\left(\nabla \cdot u_\phi\right) I \right] \tag{7}$$

$$\mu_{\phi\mathrm{eff}} = \mu_{\mathrm{lam}} + \mu_{\mathrm{T}}\,, \tag{8}$$

$$k_{\phi\mathrm{eff}} = k_{\mathrm{lam}} + k_T \tag{9}$$

Table 7. Thermophysical properties

Material	Density (kg/m^3)	Dynamic viscosity (Pa-s)	Cp (J/kg-K)	K (W/m-K)
Exhaust Gas (Air)	0.4 at p = 1 atm, T = 883 K	Sutherland's law	1,117 at 883 K	0.06179 at 883 K
Steam HPSHs	36, at p = 1763 psig, T = 896 F	Sutherland's law	2,643 at p =1,763 psig, T = 973 F	0.08 at p =1763 psig, T = 973 F
Steam RHTRs	9, at p= 426 psig, T = 821 F	Sutherland's law	1,938 at 298 K 2,244 at p = 426 psig, T = 935 F	0.0253325 at 298 K 0.07 at p = 426 psig, T = 935 F
Steel	7,840	–	490	30 at 883 K
Oxide	2,702	–	903	3

Table 8. Inlet flow conditions of HRSG

Duct exhaust flow rate	272 kg/s
HPSH1 per tube flow rate	0.53 kg/s
HPSH2 per tube flow rate	0.456 kg/s
RHTR1 and 2 per tube flow rate	0.2129 kg/s
Inlet exhaust air temperature	883 K

HPSH2 inlet temperature	751 K
RHTR1 and 2 inlet temperature	720 K
HPSH1	HPSH2 outlet is connected to HPSH1 inlet

3.3.2 Geometry and Computational Mesh

An accurate representation of the simulated HRSG (original equipment manufacturer (OEM) is Vogt Power) is given in Figure 17. The HRSG was considered to be symmetric with respect to a central plane parallel to the x-z plane (parallel to the exhaust gas flow) and thus the assumption of symmetric flow inside the HRSG along the same plane was made. A gap is present between the left and right sides delimited by the symmetry plane; therefore, only half of the geometry of the real-scale HRSG was considered for the study to reduce the computational cost. The primary objective of the current study is to examine the oxide thickness profile. The sections in the HRSG for the operational conditions simulated (no duct burner operation) that are most affected by high temperature stead-side oxidation are the high pressure superheaters (HPSHs) and reheaters (RHTRs) located nearest the inlet duct, in a location termed "Box 1", which experiences the maximum heat load. Other sections of the HRSG, including HPSH and RHTR sections further downstream in the direction of exhaust gas flow and other HX sections (e.g., evaporators, economizers, and other superheaters) located outside of Box 1 were omitted to save computational cost. Heat exchanger assemblies in Box 1 consist of finned tubes arranged in a staggered manner, as shown in Figure 18.

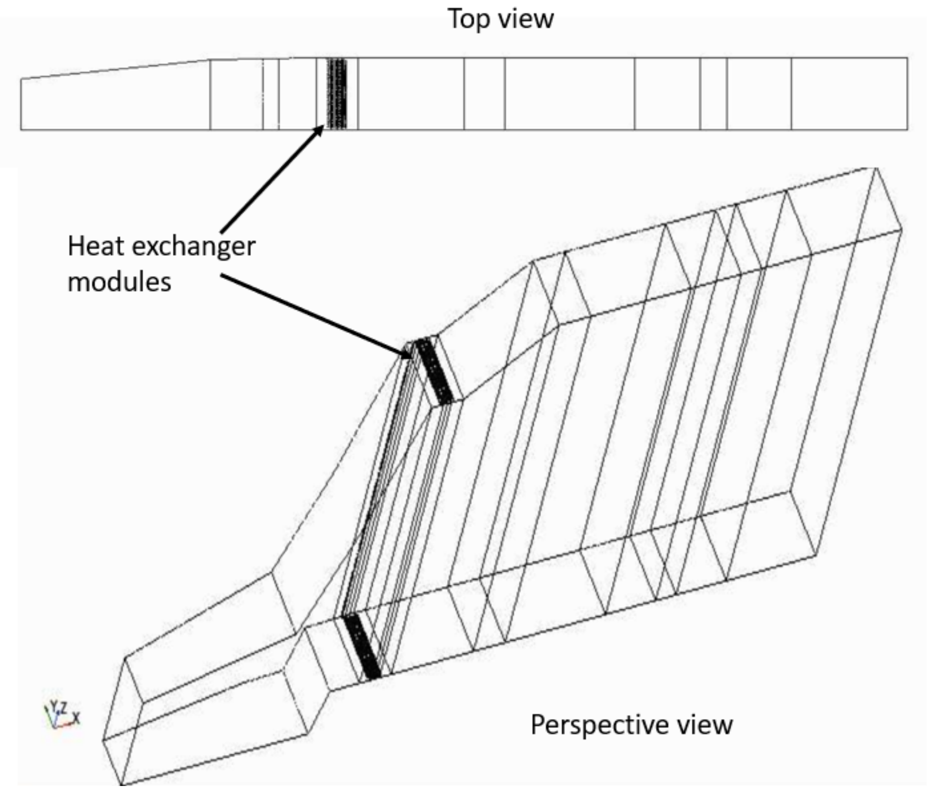

Figure 17. CAD model of real-scale half-HRSG.

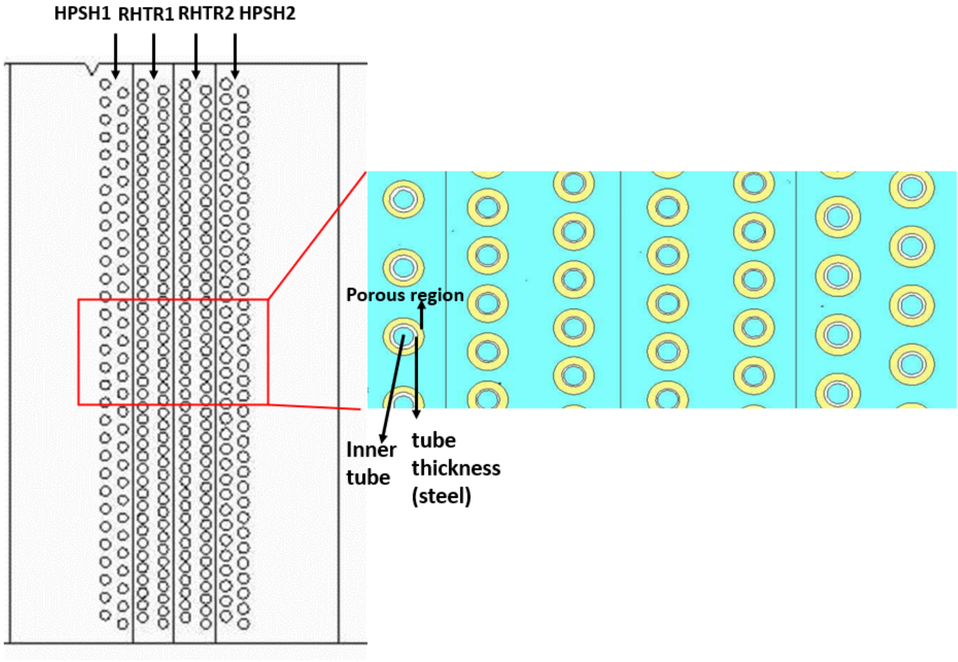

Figure 18. Top view of the HX tubes considered for oxidation study.

The polyhedral mesher in STAR-CCM+ is used to generate the mesh for the duct and the tubes. Approximately 170 million mesh elements were required to resolve the gaps between the tubes and the internal steam flow within the tubes (see Figure 19 and Figure 20). Mesh refinement beyond 170 million elements resulted in computer random access memory problems, so a mesh with refinement was used that best suited the available computational resources. Moreover, due to the limitation in the cell refinement possible, the prism layer generated inside the steam tubes are of lower quality i.e. there is a large cell jump between the prism layer and the bulk of the cells. A conformal mesh was used to accurately capture heat transfer from the exhaust gas in the duct to the steam in the tubes. Nonconformal meshes were causing solution divergence. Parallel generation of conformal mesh is not feasible in STAR-CCM+. Therefore, to reduce the meshing time and random-access memory problems, the HRSG was decomposed into multiple parts based on the sections, meshed concurrently on different cores in serial mode, and then reassembled to generate the full mesh. The results examined in the following section were obtained for the mesh with 170 million cells. The fins were not captured or resolved using the mesh; rather, they were modeled as porous regions, as described in Section 4.2.

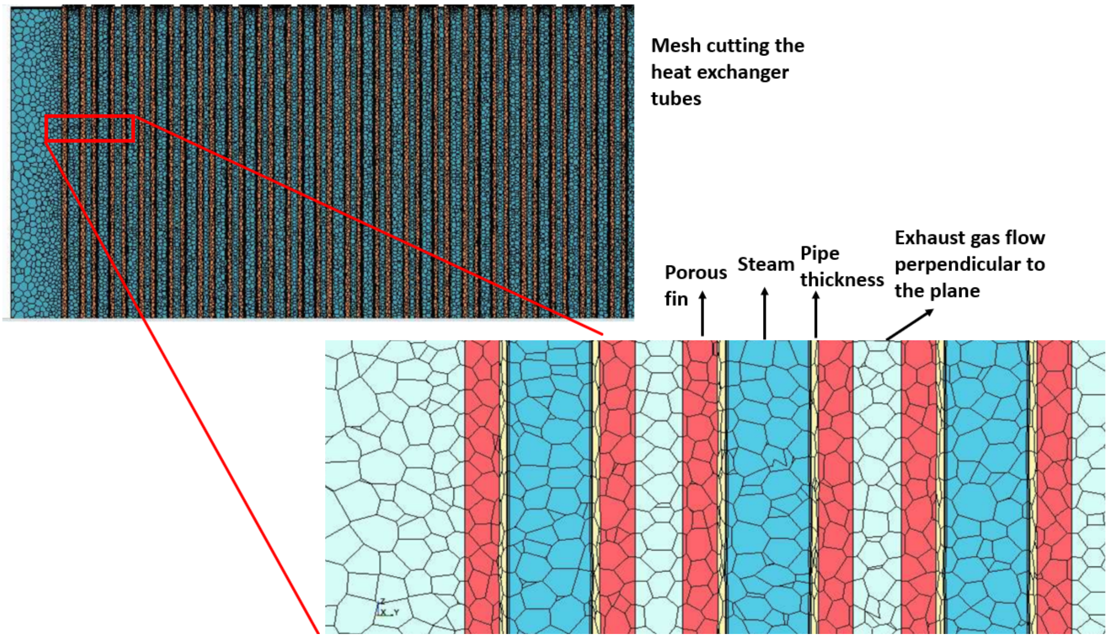

Figure 19. Mesh on a vertical plane perpendicular to the exhaust gas flow cutting the tubes.

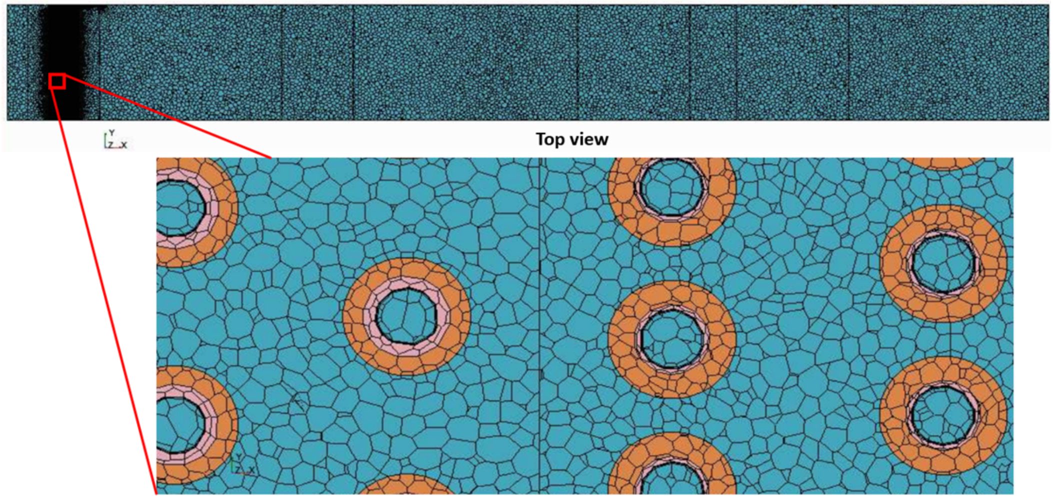

Figure 20. Mesh on a horizontal plane parallel to the exhaust gas flow cutting the tubes.

3.3.3 Tuning of Porous Media Parameters to Match Field Test Data

The porous media coefficients—porosity and conductivity used to approximate fins—were obtained from the simulation through an iterative procedure to match the outlet tube temperature test data given in Table 9 (note that steam flows from HPSH2 to HPSH1 with no temperature measurement in-between). The final coefficients that provided a reasonable fit with the test data are given in Table 10.

Table 9. Comparison of CFD vs. test data for average outlet tube temperature

Sections	CFD simulation temperature (K)	Validation data temperature (K)
HPSH1	830	830
RHTR1	829	830
RHTR2	829	830

Table 10. Porous coefficients used to match the test data

Sections	Thermal conductivity of solid phase (W/m-k)	Porosity
HPSH1/2	7	0.61
RHTR1	65	0.94
RHTR2	16	0.5

The Forchheimer parameters that control the source terms to model the effect of the fins on the pressure drop were determined using small sections of the full geometry. The pressure drop is dependent on the geometry of the fin, so one calibration study is required per fin type. The values used for the Forchheimer parameters are provided in Table 11.

Table 11. Forchheimer parameters

Sections	Viscous parameter	Inertial parameter
HPSH1	6.7159	1.849
HPSH2	40.51881455	4.601949732
RHTR1	26.74203557	4.176840191
RHTR2	72.12311926	6.779714566

3.3.4 Results and Discussion

3.3.4.1 Flow pattern inlet duct

Before it passes through the HX tubes, the high-temperature exhaust gas that comes from the gas turbine passes through an inlet duct as shown in Figure 6. The flow velocity magnitude of the exhaust gas hitting the tubes of the HX and its uniformity are two major factors—aside from the HX configuration—that determine the HRSG heat extraction efficiency. A well-designed inlet duct can help ensure gas uniformity, which can be defined as

$$UI = 1.0 - \frac{\sum_{i=1}^{n} \frac{|u_i - \bar{u}|}{\bar{u}} A_i}{2.0\, n\, A} \; and \; \bar{u} = \frac{\sum_{i=1}^{n} u_i}{n\, A}, \tag{10}$$

where u_i is the local velocity, $\bar{u}$ the mean velocity, A_i is the local cell area, and A is the total brick area. The number of cells is denoted by n. The theoretical maximum for gas uniformity index (UI, a metric for flow uniformity) is 1, which may never be achievable in HRSGs because the flow must almost always expand from the gas turbine to the HX because of the geometric scale difference. However, flow control devices such as perforated plates and baffles (Yuwono & Widodo, 2021) (Hegde, Han, Lee, & Roy, 2007) (So, Jo, Lee, Koo, & Lee, 2018) can be placed in the inlet duct to achieve a better flow uniformity at the expense of a larger pressure drop.

The inlet duct of the simulated HRSG design does not include a flow control device, but the flow is diverted upwards because of the geometry at the bottom of the duct, as seen in Figure 21 (right). This provides better flow uniformity in comparison to conditions without a diverter. The exhaust gas flow in the inlet duct expands in both y and z directions perpendicular to the flow direction, causing a swirl in the upper region of the duct, as shown in Figure 21 (top). This swirl flow is not beneficial to the uniformity, because most of the flow is passing through the region bounded by the bottom and central parts of the HX (see Figure 21 (bottom)). A small circulation cell is formed beside the bottom of the tubes close to the diverter which can negatively effect the heat transfer performance in that region.

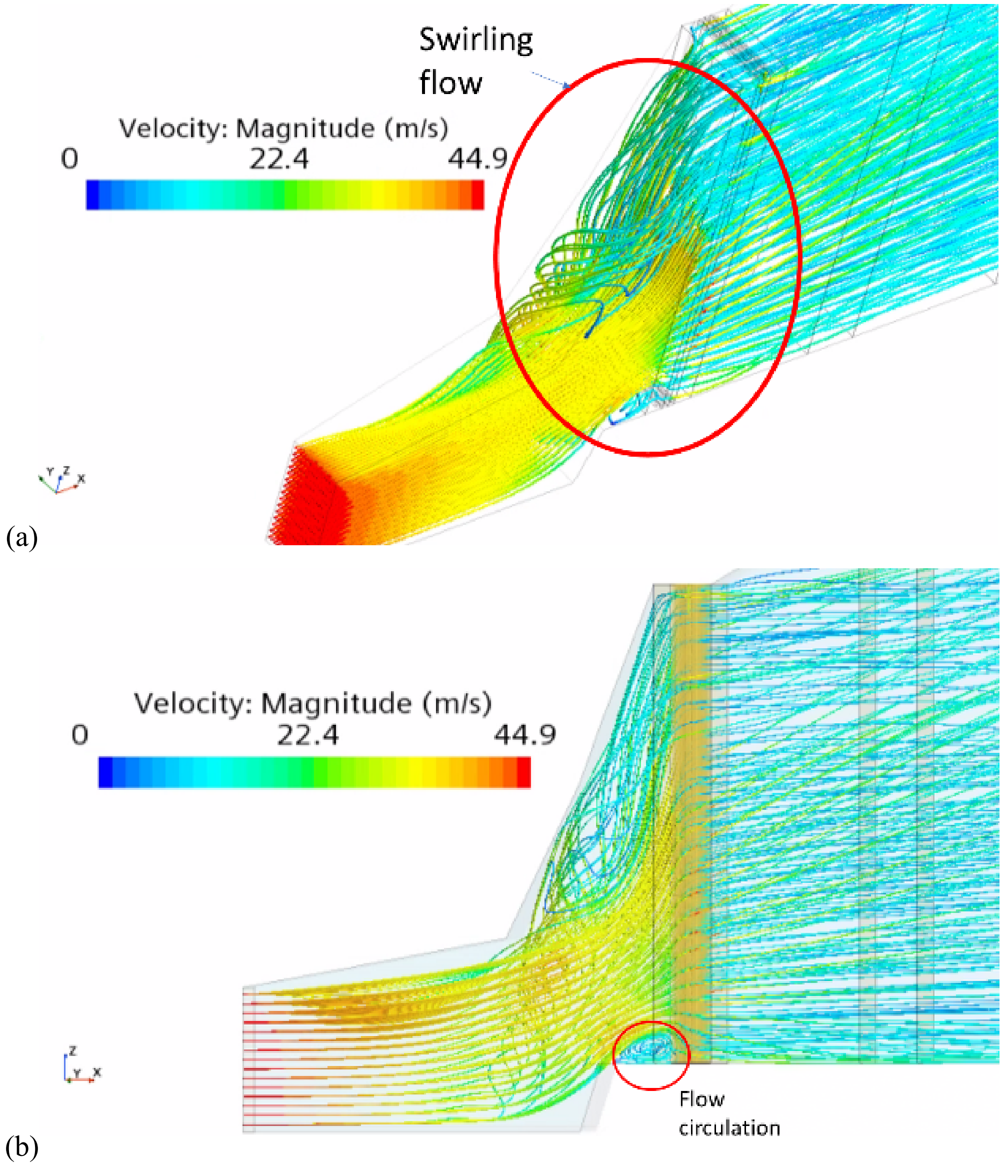

Figure 21. Flow pattern in the inlet duct of the HRSG: perspective view (a) and side view (b).

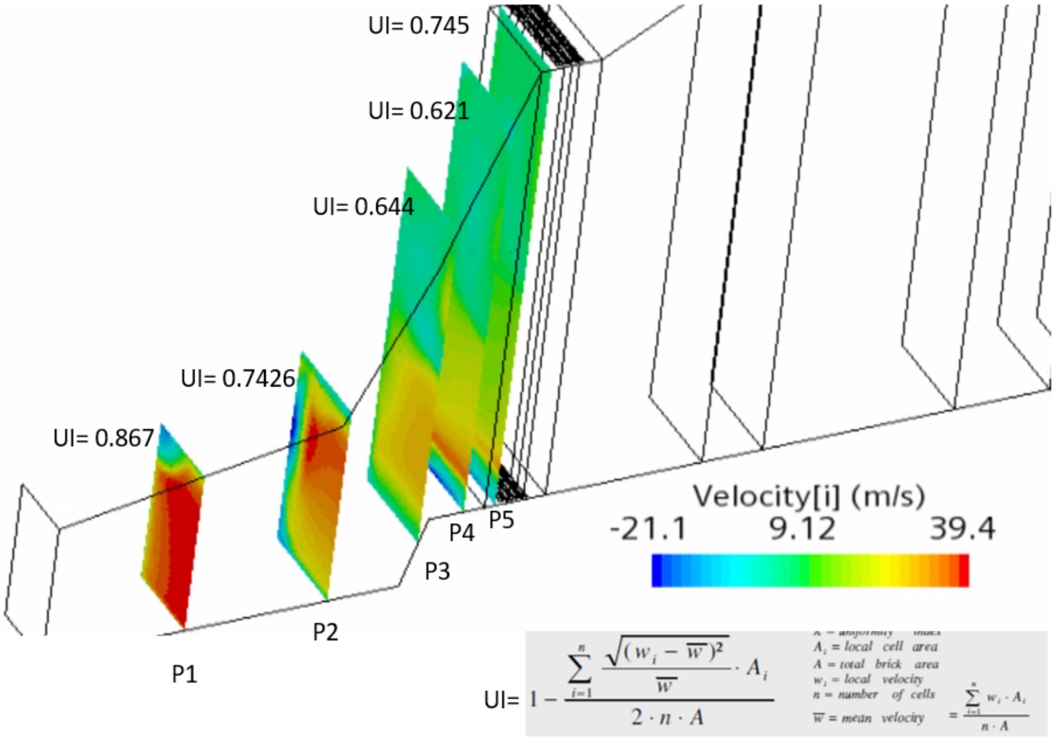

$$UI = 1 - \frac{\sum_{i=1}^{n} \frac{\sqrt{(w_i - \overline{w})^2}}{\overline{w}} \cdot A_i}{2 \cdot n \cdot A}$$

A_i = local cell area
A = total brick area
w_i = local velocity
n = number of cells
$\overline{w}$ = mean velocity $= \frac{\sum_{i=1}^{n} w_i \cdot A_i}{n \cdot A}$

Figure 22. Flow UI on different planes in the flow direction.

Figure 22 shows the evolution of exhaust gas flow velocity and UI on different planes along the flow direction until the flow enters the HX tubes. As seen in the figure, as flow evolves through the duct, the UI progressively decreases because of expansion and recirculation until the second-to the last plane, ultimately reaching a value of 0.745 just before contacting the HX tubes. The flow is also expanding in the y-direction which causes flow separation in the left side of plane P2 as shown by the negative blue region. It appears that the flow UI of 0.745 is sufficient for the needed thermal performance of the simulated HRSG. This may be the reason that there is no flow control device in the inlet duct. It should also be noted that flow control devices also cause flow energy losses, which is another reason to omit these devices in front of HX tubes.

3.3.4.2 Flow and heat transfer across HX tubes

The exhaust gas entering the inlet duct flows through the HX and transfers its heat. Figure 23 shows a 3D vector plot of the exhaust gas flow on a plane cutting the tubes parallel to the exhaust gas flow direction. The exhaust gas flow is predominantly in the upward z-direction in the inter-tube gaps of HPSH1 and RHTR1 because of the geometry at the bottom of the duct, as discussed above. The exhaust gas flow velocity needed for maximum convective heat transfer should be high in the x-direction because the z-direction velocity component does not have as large of a contribution towards convective heating of the tubes. Although the exhaust gas flow is predominant in the z-direction for HPSH1 and RHTR1, it is interesting to note that the flow shifts toward the x-direction in the RHTR2 and HPSH2 sections on this plane, as seen on the right side of the vector plot in Figure 23. Figure 24 shows the flow vectors on a horizontal plane through the top region of the HRSG. The vectors are oriented predominantly in the x-direction, or perpendicular to the tubes, and the top region of the HRSG shows a more favorable orientation of exhaust gas flow than the center plane in terms of heat transfer. However, the magnitude of the exhaust gas velocity is significantly lower compared to that in the center region.

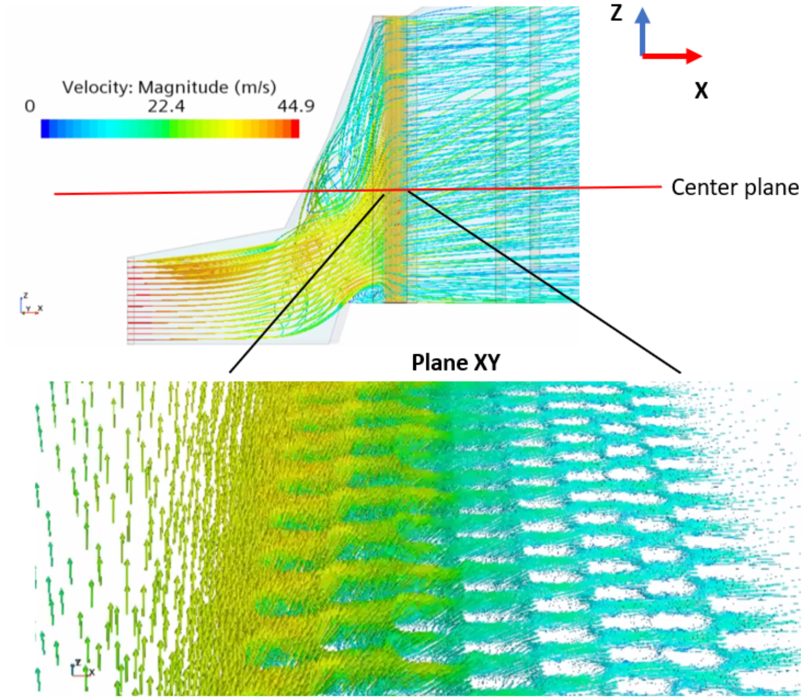

Figure 23. 3D exhaust gas flow vector on a plane cutting the tubes at the center of the HRSG.

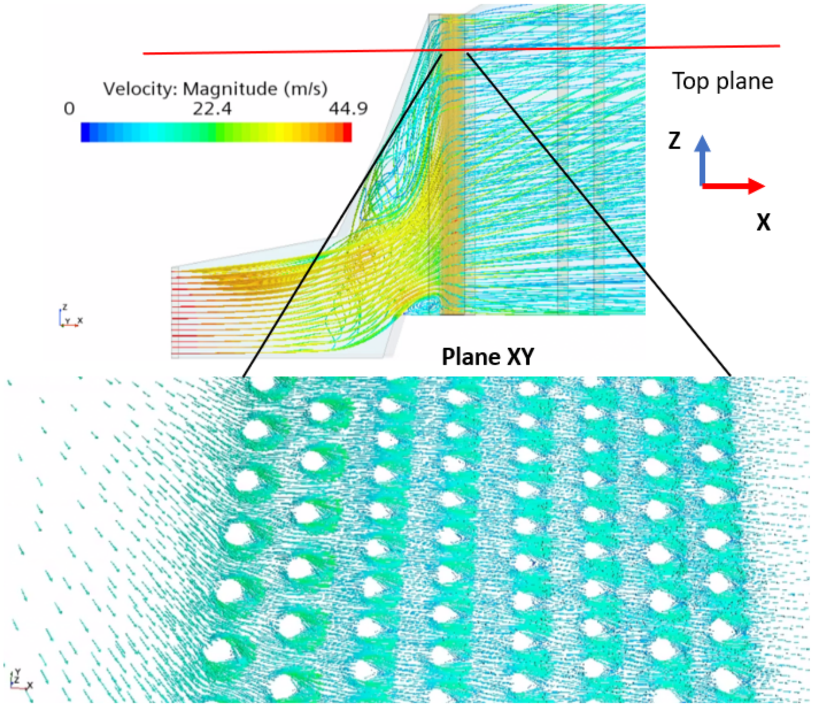

Figure 24. 3D exhaust gas flow vector across the tubes on a plane cutting the tubes at the top of the HRSG.

Figure 25 shows the velocity contour of the exhaust gas flow across the tubes on a central plane along the flow direction. The highest velocity magnitudes are found in the regions between the HX tubes and the duct walls (top of Plane XY view), as well as the regions between the HX tubes and the symmetry boundary (bottom of Plane XY view). The higher velocity magnitudes are found here because of the lower flow resistance in these regions; some of the heat energy that can be harvested escapes through these regions. Baffles can be used to redirect the flow toward the tubes to increase heat extraction. The exhaust gas flow entering the first tube section is nonuniform because of the swirl produced in the inlet duct. Therefore, the swirl formation disrupts the flow uniformity in the z- and y-directions. Improved design of the duct components can avoid such swirls and improve exhaust gas uniformity in both directions.

The streamlines across the tubes (see Figure 26) show boundary separations and associated wake formations behind the tubes. A pair of vortices can be seen behind most of the tubes. Because of the formation of vortices, the back (or downstream, in the direction of exhaust gas flow) surface of the tubes experiences lower heat loads compared to the front (or upstream) surface, thus resulting in lower oxidation growth. This is discussed in the subsequent sections in greater detail and is illustrated in line plots showing oxide thickness.

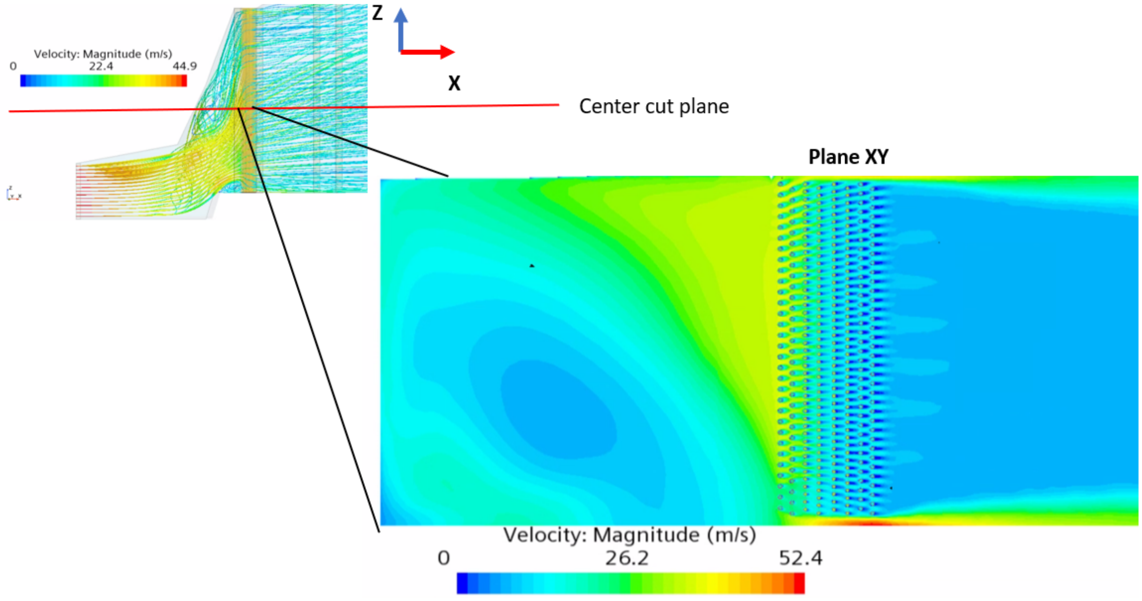

Figure 25. Velocity contour across the tubes.

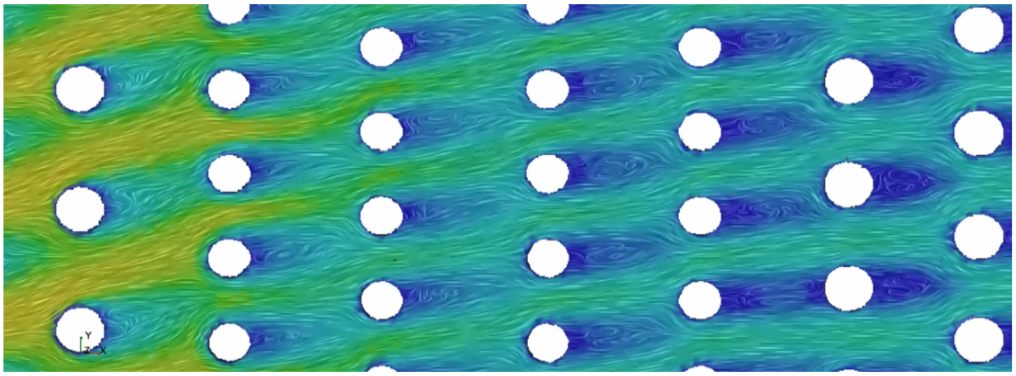

Figure 26. Streamlines.

The velocity contour indicates that the staggered arrangement of the tubes facilitates increased heat transfer as compared to the non-staggered (or in-line) arrangement. The staggered arrangement allows for maximum exhaust gas flow velocity, which results in maximum convective heating. In the non-staggered arrangement, upstream (in the direction of exhaust gas flow) tubes shield downstream tubes. However, the staggered arrangement is not favorable for mitigating oxidation, because the shielding effect in the non-staggered arrangement produces less oxidation in the shielded tubes. The staggered arrangement is however needed to maximum heat transfer.

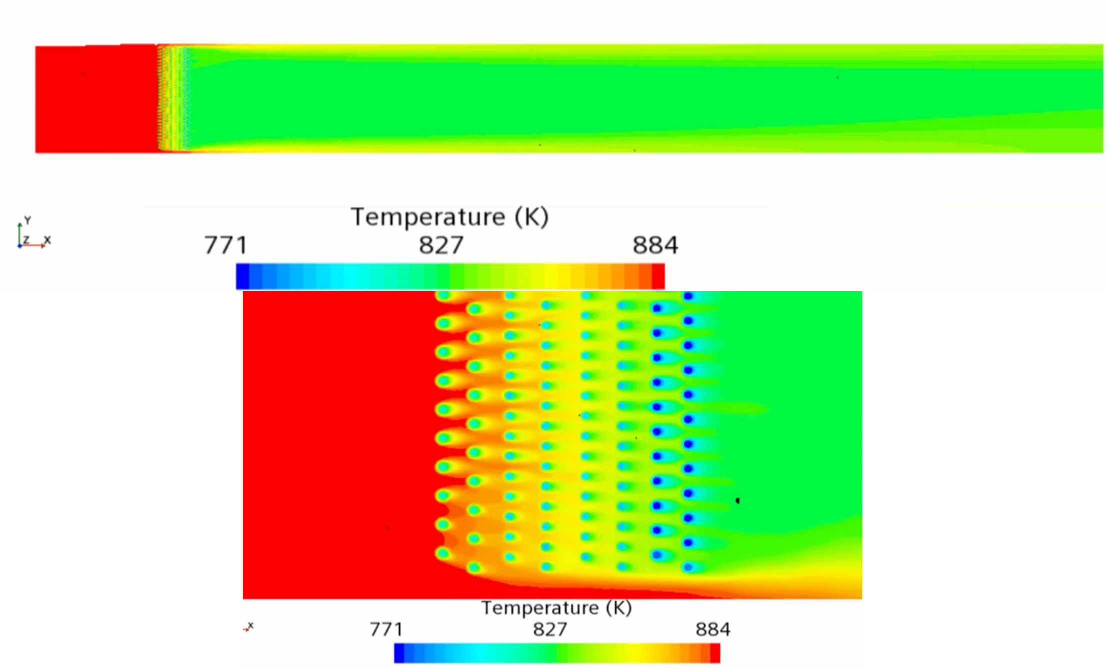

Figure 27. Temperature drops across tubes while exhaust heat is being transferred.

As the hot exhaust gas passes through the HX tubes, the hot exhaust gas transfers its heat to the relatively cold steam flowing in the tubes. The heat acquired by the steam is typically sent to the steam turbine to generate electricity. The exhaust gas exiting the tubes will have a lower temperature, as shown in Figure 27. A temperature drop of approximately 52 K is observed across the HX in the exhaust gas flow direction.

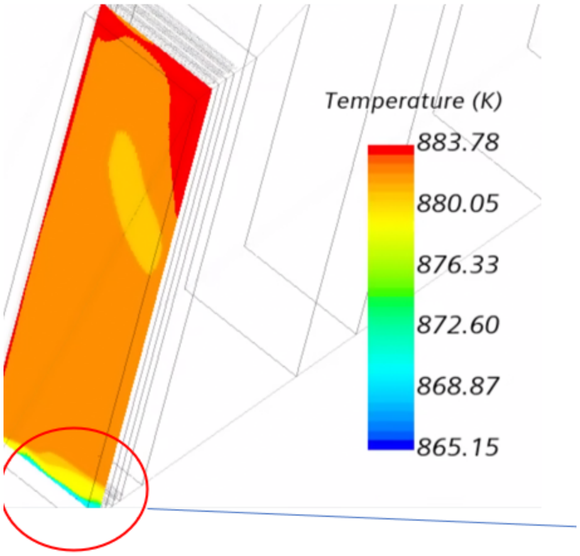

Figure 28. Temperature distribution on a plane in front of the HPSH1 tubes.

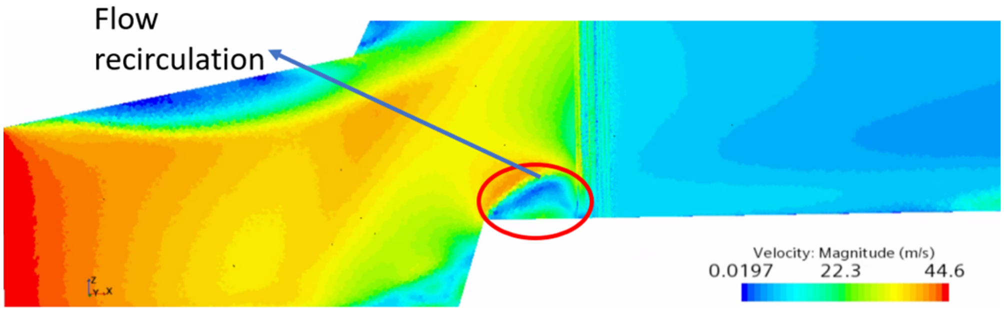

Figure 29. Exhaust gas velocity on the lower side of the HRSG.

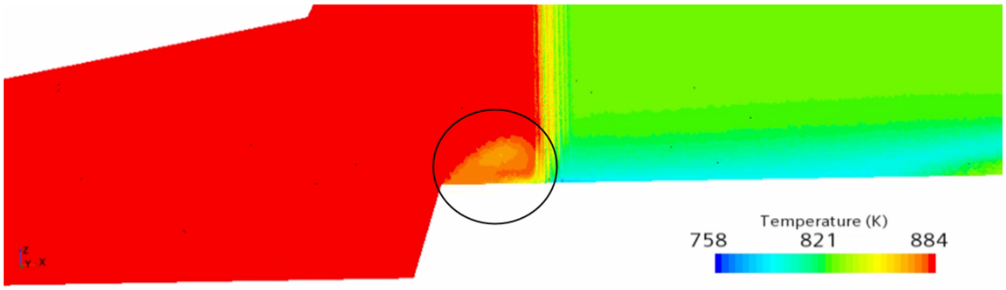

Figure 30. Exhaust gas temperature on the lower side of the HRSG.

Uniformity of the exhaust gas temperature distribution and its magnitude across the HX is also crucial for achieving high heat extraction. Figure 28 shows the temperature distribution on a plane near the entrance of the HX. A reasonably uniform temperature distribution is seen in the upper region, but a low temperature is observed in the bottom region (circled in red) near the geometry transition. The flow passing the geometry transition separates at the edge. With no time to re-attach properly, the flow forms a recirculation zone, as illustrated in Figure 29. This colder steam that enters from the bottom of the tubes extracts heat from the exhaust gas in this region. The extracted heat is never properly rejuvenated from the hot exhaust free-stream because of the recirculation (see Figure 30). Hence, a lower heat transfer rate is anticipated in this region as compared to other regions. The oxide thickness slope transitions from this region to the upper region because of the recirculation. This is discussed further in the following section.

3.3.4.3 Oxidation prediction in the tubes of different sections of HRSG

The oxide thickness variation for a tube (front or upstream side and back or downstream side, in the direction of exhaust gas flow) in the HPSH1 section along the z-direction or height of the tube is shown in Figure 31 (top). Along with the oxide line plot, Figure 31 (bottom) shows the contour of oxide thickness, exhaust gas velocity magnitude, and exhaust gas temperature for all tubes in the first row of the HPSH1 section. It can be inferred from the line plot that the oxide thicknesses for the front and backs of the tube increase along the tube height from the bottom to the top. The oxide thickness on the back of the tube is lower compared to the front, which can be explained by the formation of wakes at the back of the tubes inhibiting heat transfer, whereas the front of the tube has exhaust gas flowing predominantly normal to it. The relatively cold steam entering the bottom of each tube absorbs heat from the tube surfaces (note: tubes are heated by the exhaust gas, and steam absorbs that heat from the steel tubes). This heat absorption progressively decreases along the tube as a result of the lower temperature difference between the steam and the tube surface. The lower absorption causes a higher accumulation of heat on the tube surfaces along the direction of the steam flow, resulting in an increase in oxide thickness from the bottom to the top. The line plot of oxide thickness for the front of the tube shows a change in the slope at around 2 m from the bottom; this is caused by the small exhaust gas recirculation zone formed at the bottom of the HRSG created by the diverter (as discussed above). The correlation between the oxide thickness contour and the exhaust gas velocity magnitude contour (see Figure 31 (bottom)) near the bottom confirms this observation.

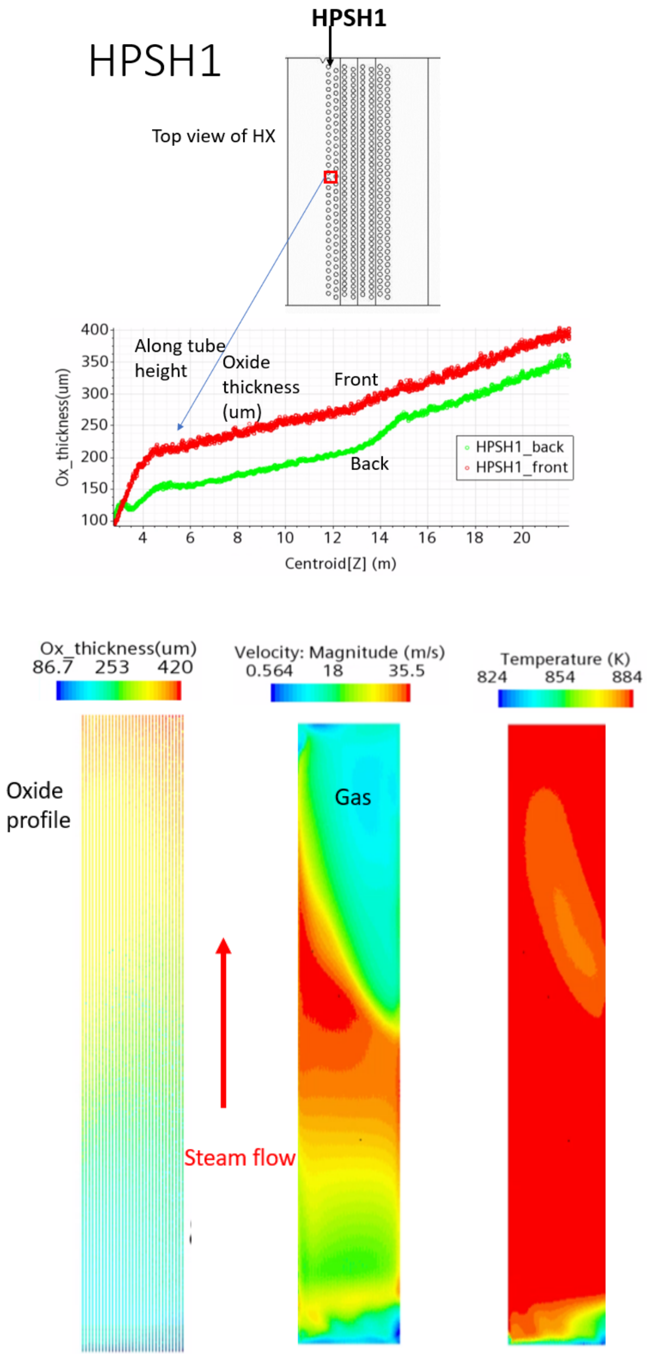

Figure 31. Oxide thickness profile along a tube in the HPSH1 section (top) and oxide thickness, exhaust gas velocity magnitude, and exhaust gas temperature contour on each tube of HPSH1 section (bottom).

The line plots showing oxide thickness and contour plots showing oxide thickness, exhaust gas velocity magnitude, and exhaust gas temperature for row 1 of RHTRs 1 and 2 are provided in Figure 32 and Figure 33, respectively. The increase in the oxide thickness along the tubes from the bottom to the top is apparent. The explanation for this behavior discussed above for HPSH1 also holds true for RHTRs 1 and 2. However, it is important to note that, unlike the oxide profile for HPSH1, the slope of the RHTR oxide thickness changes in both the bottom and top regions. The RHTR oxide thickness change in slope in the top region can be attributed to the shift in exhaust gas velocity and temperature (refer to the center and right side of Figure 32 (bottom) and Figure 33 (bottom)) along the tubes in the top region, which is caused by the swirl flow generated back in the inlet duct. It is also noteworthy that the oxide thicknesses for RHTRs are generally higher than those for HPSH1.

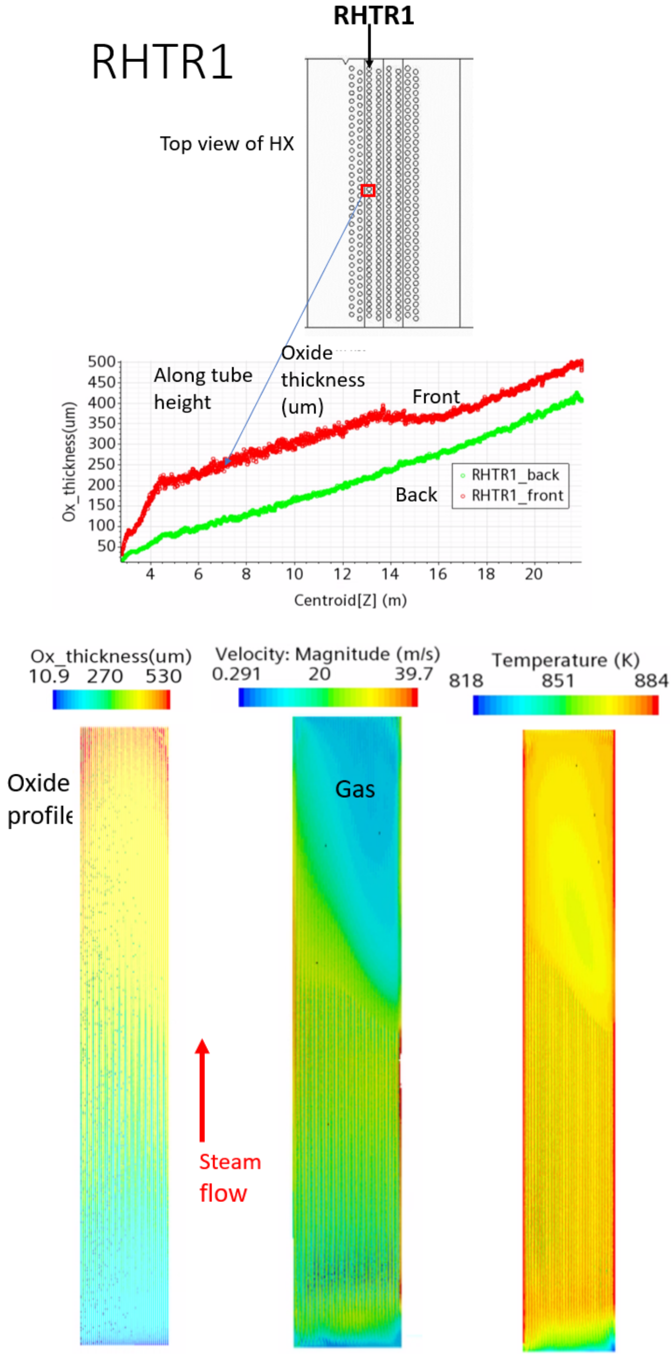

Figure 32. Oxide thickness profile along a tube in the RHTR1 section (top) and oxide thickness, exhaust gas velocity magnitude, and exhaust gas temperature contour on each tube of RHTR1 section (bottom).

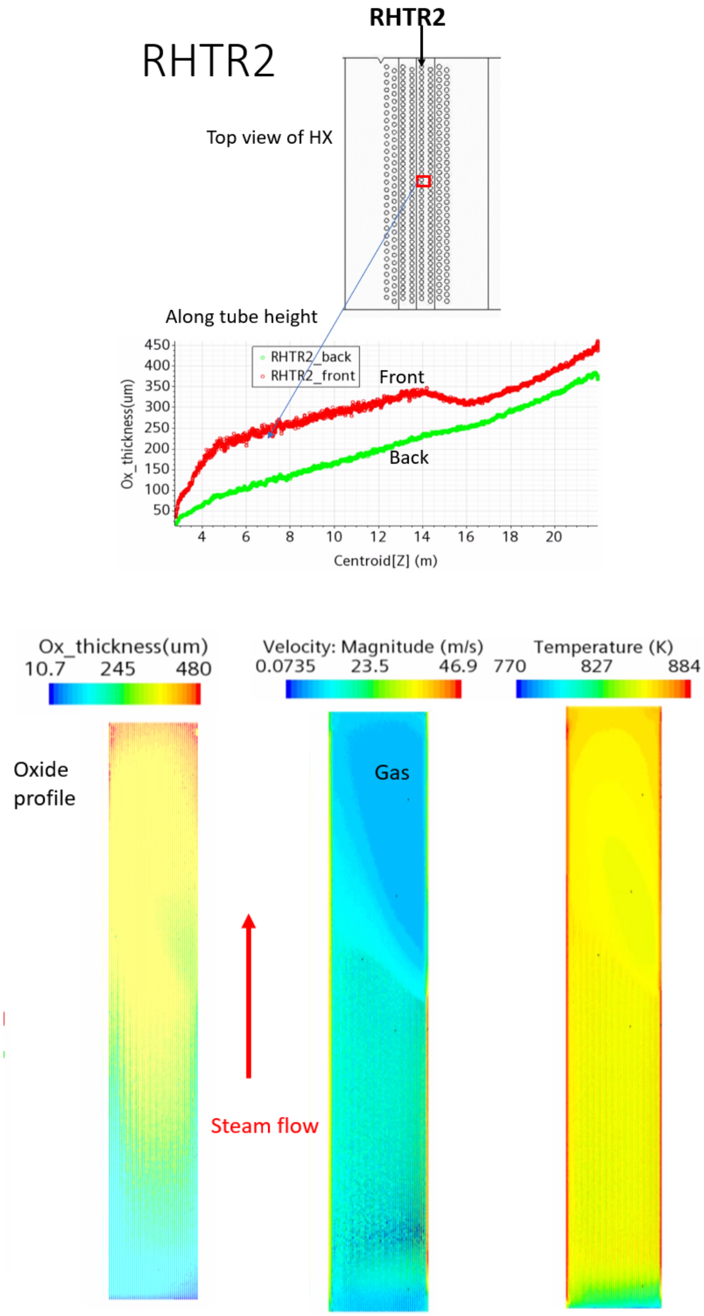

Figure 33. Oxide thickness profile along a tube in the RHTR2 section (top) and oxide thickness, exhaust gas velocity magnitude, and exhaust gas temperature contour on each tube of RHTR2 section (bottom).

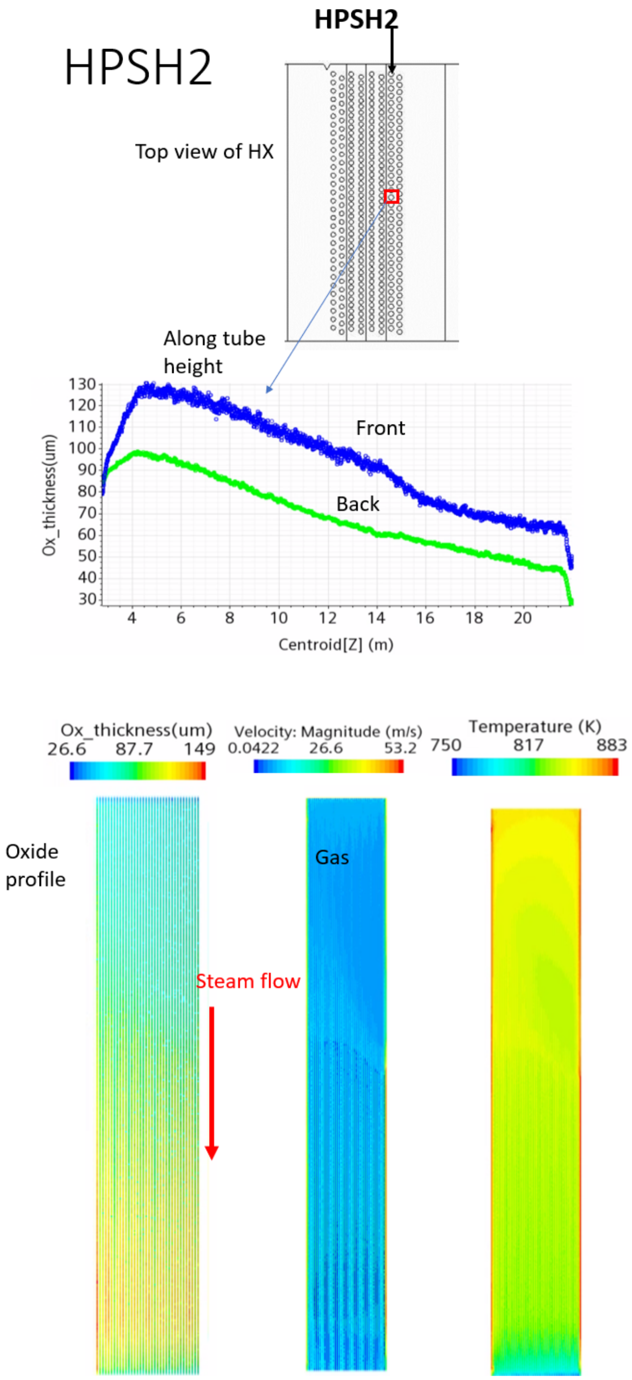

Figure 34. Oxide thickness profile along a tube in the HPSH2 section (top) and oxide thickness, exhaust gas velocity magnitude, and exhaust gas temperature contour on each tube of HPSH2 section (bottom).

The line plot of oxide thickness along a tube and the oxide thickness, exhaust gas velocity magnitude, and exhaust gas temperature contour for HPSH2 are provided in Figure 34. The oxide profiles for HPSH2 and the RHTRs show an opposite trend because the steam flows from the top to the bottom in HPSH2 (versus from the bottom to the top in the RHTRs). Near the bottom, the oxide thickness slope changes and starts decreasing because of the recirculation zone. This is apparent from the correlation between the exhaust gas temperature contour and the oxide thickness contour near the bottom. The oxide thickness in the

HPSH2 section islower than the thicknesses observed for other sections because the temperature of the exhaust gas entering this section is lower after the heat transfer that occurred in the previous sections. This results in lower heat transfer between the exhaust gas and the tubes and consequently less oxide formation than in other sections.

4. COMMERCIALIZATION POSSIBILITIES

None

5. PLANS FOR FUTURE COLLABORATION

None

6. CONCLUSIONS

EPRI and ORNL have collaborated under a Cooperative Research and Development agreement to diagnose and mitigate oxidation in the HX tubes of HRSGs—a major cause for material degradation and poor heat extraction—by leveraging CFD tools and HPC resources at ORNL. To accomplish this, a CFD framework was built in STAR-CCM+ for oxide prediction in HRSG, an innovative approach to model the effect of the fins on the heat transfer and the pressure drop based on the PMM was developed, and the oxide thicknesses in different critical sections of the HRSG's HX tubes using high-fidelity simulations were investigated.

The project consisted of three phases, as detailed below.

6.1 PHASE 1: VERIFICATION AND VALIDATION OF THE CFD MODEL ON REDUCED-SCALE GEOMETRIES

The CFD model was coupled to the oxidation model, and the oxide thickness evolution predicted by the model in a small cylindrical pipe shell was verified with Sabau and Wright's analytic model (Sabau & Wright, 2009). Then, CFD simulations were performed for a small section of finned tube banks that matched the configuration of an HX. A grid convergence study was carried out to assess the sensitivity of different flow and thermal parameters according to mesh count. After the mesh convergence study, the flow and thermal predictions were verified and validated against the heat transfer simulation (Lindell, 2019) and experimental data (Ward, 1958) for the same tube banks. Preliminary simulations were conducted to analyze the qualitative behavior of the oxide thickness evolution for bare tubes and finned tubes. The assessment of the results showed that the effect of fins on oxide thickness cannot be neglected, and the computational cost involved in capturing the fins, even for a small-scale geometry (section of tube banks), was significant. Therefore, in Phase 2, an effort was made to model the effect of fins rather than meshing and to capture the effect in a CFD simulation.

6.2 PHASE 2: MODEL DEVELOPMENT TO CAPTURE THE FIN EFFECT ON THE OXIDE THICKNESS

The PMM implemented in STAR-CCM+ was used to model the effect of the fins on the heat transfer between the gas and the steam, as well as the pressure drop in the gas flow. The computational region surrounding each pipe which was delimited by the thickness and height of the fins was treated as a mixture of solid and gas and was modeled with a porous medium approach. The Forchheimer source terms, porosity, and solid heat conductivity were calibrated to model the effect of the fins on flow and heat transfer. The pressure drops and outlet temperatures of the gas obtained in Phase 1 from the validated CFD models were used as reference values for the calibration study that was performed with the Dakota optimization package integrated to the NEAMS Workbench. The calibration process was performed on inlet conditions ranging from 4 to 32 m/s. Results show that the pressure drops and the gas outlet temperatures predicted by the PMM are within a few percentages of the reference values for all inlet conditions. The temperature profile on the inner surface of the pipe was also compared and showed very little discrepancies, most of which were located near the inlet and outlet surfaces of the pipe near the open boundary conditions. Note that accurately predicting the temperature on the inner surfaces of the pipes is crucial for modeling the oxide growth that is a temperature-driven phenomenon. Phase 2 demonstrated that the PMM available in STAR-CCM+ can (1) accurately model the effect of the fins on the heat transfer and the pressure drop, and (2) can reduce the necessary computational work. Use of the PMM reduced the mesh element count by a factor of 9. The PMM with calibrated source terms was then used in Phase 3 to model a real-scale HRSG and to predict oxidation growth on the inner surfaces of the pipes.

6.3 PHASE 3: INVESTIGATION OF FLOW, HEAT TRANSFER, AND OXIDATION IN A REAL-SCALE HRSG

The CFD model, oxidation model, and the porous fin model that were verified and validated in the previous phases were used to perform a high-fidelity simulation of a plant-scale or real-scale HRSG with the tubes of the HX sections that are most susceptible to oxidation. A detailed investigation of the flow and the heat transfer pattern within the HRSG was performed, along with the assessment of oxide growth in each HX section of the HRSG. The hot exhaust gas flow entering the inlet duct swirls as a result of the expansion of the duct, causing a reduction of exhaust gas flow uniformity across the HX in both directions perpendicular to the flow. In contrast with other studies, no flow control devices were used inside the duct to improve uniformity. However, the bottom geometry transition of the duct effectively diverted the flow to the center of the HX sections, which otherwise would have passed through the bottom of the HX. Hence, this bottom geometry transition slightly aids in achieving uniform flow across the HX. The current configuration of the inlet duct geometry provides uniformity of exhaust gas flow with a UI (a metric to measure the uniformity with maximum at 1) 0.74. Flow control devices were not used. In addition to the swirl, a small recirculation zone was formed at the bottom of HRSG near the HX section after the geometry transition. The diverted flow did not have sufficient distance to reattach itself before it entered the HX and hence created a recirculation zone. This recirculation zone, along with swirl flow, effected the heat transfer in the HX, and it also effected oxide thickness. Study of the flow and heat transfer across the HX tubes revealed that the staggered arrangement of tube banks used in the current design of HX yielded better convective heating than that of a non-staggered (or in-line) tube bank arrangement in which upstream (in the direction of exhaust gas flow) tubes shield downstream tubes from the exhaust gas flow. The staggered arrangement that promotes heat transfer exchange, however, increases formation of oxides in the tubes as a result of higher heating.

Investigation of oxide thicknesses for various HRSG HX sections revealed an increase of oxide thicknesses along the tubes in the direction of the steam flow (height-wise from bottom to top for HPSH1, RHTR1, and RHTR2, and from top to bottom for HPSH2) for all the sections. The oxide thicknesses for the RHTRs were found to be higher than those for HPSH1. Furthermore, the tubes in HPSH2 had the least oxide thickness compared to all other sections, which was as expected because the exhaust gas had already transferred some of its heat to the sections upstream (in the direction of exhaust gas flow). The back (or downstream, in the direction of exhaust gas flow) of the tubes in all the sections had low oxide thicknesses compared to the front of the tubes, because of the wake formation and low heat transfer at the back of the tubes. A slope change for oxide thickness was also observed for RHTRs from the swirl at the top and the recirculation zone at the bottom.

7. REFERENCES

Adams, B. B. (November 2021). *Dakota, A Multilevel Parallel Object-Oriented Framework for Design Optimization, Parameter Estimation, Uncertainty Quantification, and Sensitivity Analysis: Version 6.15 User's Manual.* SAND2020-12495: Sandia Technical Report.

Delchini, M.-O., Swiler, L., & Lefebvre, R. (2021). "Extension of the NEAMS Workbench to Parallel Sensitivity and Uncertainty Analysis of Thermal Hydraulic Parameters Using Dakota and Nek5000." *Nuclear Engineering and Technology*, 3449–3459.

Eca, L., & Hoekstra, M. (2014). A Procedure for the Estimation of the Numerical Uncertainty of CFD Calculations Based on Grid Refinement Studies. *Journal of Computational Physics, 262*, 104–130.

EPRI. (2017). *Guide to Grade 91 Use Temperature Limits Due to Steam Oxidation and Exfoliation.* Palo Alto: 3002011137.

Erikson, E. V. (2017). *Heat Recovery Steam Generator Technology.* Woodhead Publishing, Elsevier.

Hegde, N., Han, I., Lee, T. W., and Roy, R. P. (2007). Flow and Heat Transfer in Heat Recovery Steam Generators. *Transactions of ASME, 129*, 232–242.

Khosshal, A., Rahimi, M., Gharamani, A., & Alsairafi, A. (2011). Computational Fluid Dynamics Modeling of High Temperature Air Combustion in an Heat Recovery Steam Generator Boiler. *Korean Journal of Chemical Engineering, 28.5*, 1181–1187.

Lindell, I. (2019). *Analysis of the Flow of Secondary Steam through a Reheater Using 3D CFD.*

Panicker, N., Delchini, M., Sambor, T., Sabau, A., & Jain, P. K. (2021). Advanced Thermal-Hydraulic Model of Heat Recovery Steam Generators. *5th Thermal and Fluids Engineering Conference.* New Orleans.

Sabau, A. S., & Wright, I. G. (2009). On the Estimation of Thermal Strains Developed during Oxide Growth. *Journal of Applied Physics, 106*(2).

Shin, H., Kim, D., Ahn, H., Choi, S., & Myoung, G. (2012). Investigation of the Flow Pattern in a Complex Inlet Duct of a Heat Recovery Steam Generator. *Energy and Power, 2*, 1–8.

Siemens Digital Industries Software. (2021). *Simcenter STAR-CCM+, version 2021.1.*

So, H. K., Jo, T. H., Lee, Y. H., Koo, B. C., & Lee, D. H. (2018). Design Optimization of HRSG Inlet Duct Geometry for Improving Flow Uniformity Using Meta-Heuristic Algorithm. *Journal of Mechanical Science and Technology, 32*(2), 947–958.

Torresi, M., Saponaro, A., Camporeale, S. M., & Fortunato, B. (2008). CFD Analysis of the Flow through Tube Banks of HRSG. *Turbo Expo: Power for Land, Sea and Air, 43178*, 327–337.

Ward, D. (1958). *Heat Transfer and Pressure Drop of Air in Forced Convection across Triangular Pitch Banks of Finned Tubes.* University of Michigan.

Yuwono, E. A., & Widodo, W. A. (2021). Numerical Study to Improve Fluid Flow Patterns in HRSG by Using a Turning Vane and a Combination of Using a Turning Vane with Transition Zone Geometry Modification. *In IOP Conference Series: Materials Science and Engineering, 1096*(1), 012104 (Adams, November 2021).